IN-34

117609

p-41

# Breakdown of the Karman Vortex Street Due to Forced Convection and Flow Compressibility

Shu-cheng Chen
*Lewis Research Center*
*Cleveland, Ohio*

July 1992

**NASA**

# BREAKDOWN OF THE KARMAN VORTEX STREET DUE TO FORCED CONVECTION AND FLOW COMPRESSIBILITY

By SHU-CHENG CHEN

*NASA Lewis Research Center*

*Cleveland, Ohio 44135, U.S.A.*

## ABSTRACT

Low speed compressible flow around a heated/cooled circular cylinder has been investigated. The phenomenon of sudden disappearing of the Karman vortex street, observed in the experiment of Noto et al., was numerically simulated and studied. It was found that breakdown of the vortex street at $Re_d$=100 and $M_\infty$=0.3 is primarily an effect of forced convection. The contribution of natural convection to the current event is inconsequential. The exact mechanism of this phenomenon is unknown. However, the reason for the breakdown of vortex street is believed to be due to a high temperature zone in the wake generated by high level of wall heating. This produces an effectively lower Reynolds number flow in the near wall region when a compressible gaseous media is used. Vortex shedding stops for a reason similar when flow Reynolds number is reduced globally below its minimum value. These contrast to the results of Noto et al., who argued that the buoyancy effect was the driving mechanism of the vortex breakdown. In the current study, periodic vortex sheddings were observed when the wall heating ratio was less than 0.6. In that region, the coefficient of lift decreased sharply to zero, drag increased slowly, and the Strouhal number and Nusselt number reduced monotonically with respect to the wall heating. When the heating ratio was greater than or equal to 0.6, vortex shedding stopped. And steady flows with symmetric twin trailing vortices were observed. In this region, both the lift and the Strouhal number remained zero, the drag increased sharply, and the Nusselt number maintained the same decreasing slope as the one obtained from the previous region. Many of these characteristics are instictively different

from the numerical results presented by Chang and Sa, who simulated the vortex breakdown phenomenon by using a mathematical model for an incompressible buoyancy dominated flow. In this paper, quantitative results such as Strouhal number, lift, drag, and Nusselt number, as well as qualitative results such as streamline, isothermal, and vorticity contours obtained at various flow conditions are presented and compared with results of Noto et al. and Chang et al.. Contrasts between the two are discussed.

## 1. INTRODUCTION

Breakdown of the Karman vortex street (named by Noto) behind a circular cylinder due to buoyancy effect was observed experimentally by Noto, Ishida and Matsumoto (1985), and was simulated numerically by Chang and Sa (1990). In their works, the flow was considered to be incompressible and the structure of the flow was altered by heating or cooling the surface of a cylinder. Mathematically, the momentum of an incompressible flow can be influenced by changing the surface temperature only through the effect of buoyant force. Since the Grashof number of flows in Noto's work were as large as $3 \times 10^5$ and in Chang's work, as large as 1500, the cases investigated by them were dominated by the buoyancy effect. Breakdown of the vortex street and eventually sudden termination of the vortex shedding observed from their studies were undoubtably a direct consequence of natual convection.

The effect of wall heating and cooling on the global instability, such as the occurances of Karman vortex streets, for convection dominated compressible flows has not been studied in extent in the past. The purpose of the present work is to explore the influence of wall temperature and temperature gradient on the phenomenon of periodic vortex shedding, generated by flow over a circular cylinder, under the overwhelming effect of flow convection. At a freestream Mach number ($M_\infty$) of 0.3 and Reynolds number ($Re_d$, based on the diameter of the cylinder) of 100, forced convection and the flow compressibility are now the dominating factors for the change of momentum due to wall temperature effects. Buoyancy was proven to be inconsequential (the Grashof numbers in the present work were no greater than $2 \times 10^{-4}$). The sudden termination of vortex shedding was observed in this work when a surface heat-

2

ing ratio, $(T_w - T_0)/T_w$ reached a value of 0.6. For $(T_w - T_0)/T_w$ less than 0.6, the flows exhibited stable vortex shedding phenomenon with constant periodicity. For $(T_w - T_0)/T_w \geq 0.6$, steady flows with symmetric twin trailing vortices were observed. Considerable amount of differences in flow structures (streamline and isothermal contours) and in flow properties (Strouhal number and Nusselt number) as a function of the wall heating/cooling ratio were obtained under the present study in comparison with those presented by Chang and Sa. It is not surprising that current results do not agree with those obtained by Chang and Sa, since the driving mechanism for flows considered in this work is totally different from theirs. It is important to note, however, that the sudden disappearing of vortex streets can be obtained under completely different mathematical models. Results from the present work not only have demonstrated this point, but also have indicated the flow Mach number is one of the major parameters in affacting the global instability. Characteristics of the flow obtained from the investigation of an incompressible flow may not be applicable to a compressible flow even if they have similar physical appearances.

## 2. MATHEMATICAL FORMULATION

Two dimensional simulations of flow around a circular cylinder with constant surface temperature $(T_w)$ were performed by solving a set of compressible Navier-Stoke equations. The set of equations is well known and is presented here only in its symbolic form as

$$\frac{\partial \mathbf{Q}}{\partial t} + \frac{\partial \mathbf{E}}{\partial x} + \frac{\partial \mathbf{F}}{\partial y} = \frac{\partial \mathbf{E_v}}{\partial x} + \frac{\partial \mathbf{F_v}}{\partial y} + \mathbf{G}, \tag{1}$$

where vectors $\mathbf{Q}$, $\mathbf{E}$, $\mathbf{F}$, $\mathbf{E_v}$, $\mathbf{F_v}$ and $\mathbf{G}$ are defined as

$$\mathbf{Q} = (\rho, \rho u, \rho v, E_t)^T,$$

$$\mathbf{E} = (\rho u, \rho u^2 + p, \rho uv, (E_t + p)u)^T,$$

$$\mathbf{F} = (\rho v, \rho uv, \rho v^2 + p, (E_t + p)v)^T,$$

$$\mathbf{E}_v = (0, \tau_{xx}, \tau_{xy}, u\tau_{xx} + v\tau_{xy} + q_x)^T,$$

3

$$\mathbf{F}_v = (0, \tau_{xy}, \tau_{yy}, u\tau_{xy} + v\tau_{yy} + q_y)^T,$$

$$\mathbf{G} = (0, -\rho g, 0, -\rho g u)^T.$$

Equation (1) was transformed into a generalized coordinate system and was integrated by an implicit factorized scheme developed by the author and his co-workers. Only important features of this numerical technique will be listed here. Details of the scheme can be found in the paper by Chen, Liu and Kim (1991).

The factorized sheme produces the following equation

$$\mathbf{L}\delta\mathbf{Q} = -\frac{\partial \mathbf{Q}}{\partial t} - \frac{\partial \mathbf{E}}{\partial x} - \frac{\partial \mathbf{F}}{\partial y} + \frac{\partial \mathbf{E_v}}{\partial x} + \frac{\partial \mathbf{F_v}}{\partial y} + \mathbf{G}, \tag{2}$$

where $\mathbf{L}\delta\mathbf{Q}$ represents linearization and factorization error of the scheme. Solution of the nonlinear, unsteady Navier-Stoke equation (the RHS of (2)) was achieved by integrating Equation (2) with a constant physical time step. Within each step, a recursive, inner Newton iteration process was adapted to eliminate residue of the integration expressed by the LHS of (2). Three iteratiors were used for every physical time step. Simulation was stopped when the limit cycle of the shedding pattern had been well established or when the symmetric twin vortices were observed for a steady flow. Under either situation, the Root-mean-square residue of (2) at the final stage was controlled to be of the order of $10^{-5}$ for all cases presented in this work.

The time derivative $\frac{\partial \mathbf{Q}}{\partial t}$ was approximated by a four time-level backward differencing form with a third order accuracy. Spatial derivatives of the inviscid flux were formulated by a hybrid sheme, which contains a third order upwing differencing Roe scheme and a fourth order central differencing scheme with equal contribution from both forms. Under this hybrid scheme, numerical dissipative and dispersive errors were well controlled without the need of alien damping terms such as artificial viscosities. Viscous flux terms were approximated by a second order central differencing in a strong conservation form. The leading truncation error of each term in the RHS of (2) was a fourth derivative functional, so that the numerical error from discretization generated by each term would not contaminate one another physically.

Air was the media used in this study. The ideal gas law was assumed to hold, i.e.,

4

$\gamma$=1.4 and p=$\rho$RT. The molecular viscosity was assumed to obey the Sutherland's law. The Prandtl number was specified at a constant value of 0.75. The molecular thermal conductivity followed the same functional behavior with respect to temperature as the molecular viscosity. The freestream temperature ($T_0$) was set at 306°K, and the air density was 1.2272$k_g$ /$m^3$.

Properties of the flow, that is the lift coefficient ($C_l$), drag coefficient ($C_d$), Nusselt number (Nu) and Strouhal number (S) used in the work are defined as

$$C_l = Lift/(0.5\rho_\infty U_\infty^2 \cdot d),$$

$$C_d = Drag/(0.5\rho_\infty U_\infty^2 \cdot d),$$

$$Nu = -(\frac{\partial T}{\partial n})_w \cdot d/(T_w - (1+\frac{\gamma-1}{2}M_\infty^2)T_0),$$

$$S = \frac{d/U_\infty}{T_p};$$

The subscript $\infty$ represents the freestream value. $T_p$ is the shedding period and d is the diameter of the cylinder.

## 3. DOMAIN DECOMPOSITION AND BOUNDARY CONDITIONS

The computational domain was an annular with an inner circle of radius $l$ representing the cylinder, the outer boundary was placed at a distance of 61$l$ from the center. 121 points were used in the radial direction and 62 points in the circumferential direction with 1 point on each end overlapping across the trailing edge branch cut (see Figure 1). Spacing of the grids in the circumferential direction was uniform. The grid spacing in the radial direction was stretched by a hyperbolic sine function so that grids were clustered near the cylinder surface.

To avoid the effect of boundary blockage, the finding of a suitable distance for the outer boundary is important. In the paper by Jordan and Fromm (1972), a distance of 187$l$ was used for the outer boundary. Borthwick (1986) suggested 80$l$ to be the safe distance. Chang

5

and Sa used $25l$ togather with a set of analytical correction terms to the freestream conditions to prevent the effect of boundary blockage. The author started with a distance of $25l$ for the outer boundary and obtained an oscillatory highly Mach number dependent phase lag in the lift coefficient-to-drag coefficient $(C_l\text{-}C_d)$ relation (see Figure 2). It was not untill the outer boundary were moved to the present location $(61l)$ that the phase lag observed from the $C_l\text{-}C_d$ diagram had become nearly uniform and close to the value observed by Jordan and Fromm (the phase lag in the present study is about $225^\circ$ while that at Jordan and Fromm was $240^\circ$). Details about the $C_l\text{-}C_d$ phase lag will be discussed in Section 4.2. Further increase of the outer radius would have affected the accuracy of the calculation therefore the outer boundary was set at the present location.

To avoid the reflection of various type of waves from the outer boundary, a set of boundary conditions based on the one-dimensional Reimann Invariants and the streamline compatibility conditions were used. More specifically, upstream

$$R_2 = \mathbf{V} \cdot \mathbf{n} - \frac{2c}{(\gamma - 1)},$$
$$R_4 = \frac{p}{\rho^\gamma},$$

were specified ($\mathbf{n}$ represents the surface outward normal), and

$$R_1 = \mathbf{V} \cdot \mathbf{n} + \frac{2c}{(\gamma - 1)},$$
$$R_3 = \mathbf{V} \cdot (\mathbf{k} \times \mathbf{n}),$$

were extrapolated from the interior with a simple relation that $\mathbf{R}^n = \mathbf{R}^{n-1}$. The n and n-1 are a pair of points located at the end of radial line. Downstream, $R_1$, $R_3$, and T were extrapolated from the interior while p was given the freestream value.

The upstream and downstream boundary conditions are different because of the requirement of the flow being inviscid and isentropic that is inherent to the Reimann Invariants and to the streamline compatibility conditions is not strictly satisfied in the wake at the outlet plane. As a result, when the surface of the cylinder was heated up to a certain level, numerical instability was encountered. This problem was not observed, however, when the current

6

outflow conditions were applied.

At the solid wall, the no slip condition, the scaler momentum relation (scaler momentum is the dot product of surface norm to the vector momentum), and the constant wall temperature condition were used. Periodic boundary conditions were used on the overlapped boundary lines across the trailing edge cut. The potential problem of boundary values lagging in time due to application of explicit boundary conditions was effectively relieved by the use of Newton iteration process which renews boundary relations at every inner iteration.

## 4. RESULTS AND DISCUSSION

### 4.1 Baseline Performance Test

The main focus of this work is the breakdown of the vortex street behind a circular cylinder in a convection dominated compressible flow. Before the vortex shedding phenomenon was studied, the adequacy of the present numerical scheme and mesh system was first assessed. A comparison was made with experimental measurements made by Eckert and Soehugen (1952), in which Nusselt numbers for flows over an unheated circular cylinder were reported. The freestream Mach number of the current test was 0.1. The Reynolds number was 23, which is below the minimum Reynolds number for periodic shedding to occur. Calculations with a wide range of wall temperatures were conducted to study the heating and cooling effect on steady flows. The outcome of these tests is crucial in supporting results obtained from the vortex breakdown calculations that will be presented later in this section. All calculations were started implusively. Gravitational effect was not included in these flow simulations.

Figure 3(a) shows the local Nusselt number (Nu) along the cylinder wall under various wall temperature conditions in comparison with the measurements made by Eckert and Soehugen at $Re_d=23$. In their experiment, an unheated wall was considered. Since the speed of the flow was low ($M_\infty \sim 0.02$), the surface temperature ($T_w$) of the unheated cylinder should be very close to the freestream temperature ($T_0$). The present results at $T_w \sim T_0$ show good agreement with Eckert and Soehugen's measurement. The contours of the Nu for the current

calculation with $T_w = 1.05 \, T_0$ and $T_w = 0.95 \, T_0$ actually bounded the contour of the measured Nu, except near the trailing edge region. In that region, the measured results were not only asymmetric but also showed a anomalous increase near the trailing edge point. I have observed the increasing trend in my results only in the early stage of simulation, when the steady state had not nearly been reached. The asymmetrical behavior was not observed in the calculations.

Figure 3(b) shows the global Nusselt number, which is the integrated value along the cylinder wall, versus the wall temperature variation. Notice the decreasing trend of $Nu_g$ with respect to the heating ratio $(T_w - T_0)/T_w$ when a compressible gaseous media was used. Eckert and Soehugen's measurement is marked in the figure for comparison. As expected, the measured value is in close agreement with the current value of $Nu_g$.

Figure 3(c) shows the drag coefficient $C_d$. $C_d$ exhibited a rising trend with respect to wall heating. Measurement made by Tritton (1959) is marked in the figure for comparison. The measurement at $M_\infty \sim 0.01$ matchs the current $C_d$ reasonably well.

Figure 4 illustrates the steady symmetrical pattern of the flow by showing the isothermal contours obtained from the present calculation for cases of $T_w = 0.9 \, T_0$ and $T_w = 1.1 \, T_0$.

## 4.2 Periodic Vortex Shedding

To justify the present approach to situations when periodic shedding occurred, further tests were made at the flow conditions of $Re_d = 100$ and $(T_w - T_0)/T_w = 0.1$. Four different freestream Mach numbers 0.1, 0.2, 0.3 and 0.4 were calculated. Non-dimensionalized time steps $\Delta t = 0.015, 0.025, 0.04$ and $0.04$ were used for the four cases respectively. At lower Mach number, the algebraic system stiffness matrix becomes ill-conditioned. This reduces the effectiveness of Newton iteration process in controlling the residue. To make sure at least the same level of convergence was achieved in comparison to other cases, two extra inner iterations were given to cases of $M_\infty = 0.1$ and 0.2. This made the total number of iterations per time step five for these two cases only. Gravitational force was included in the calculations. Flow simulation was stopped after the limit cycle of the periodic shedding had

8

been well established.

The lift coefficient-to-drag coefficient ($C_l$-$C_d$) phase diagrams are shown in Figure 5. The time dependent global Nusselt numbers ($Nu_g$) are shown in Figure 6. To understand the underlying physics involved in these near wall properties of the flow, a simple Fast-Fourier-Transformation (FFT) was performed on $C_d$, $C_l$ and $Nu_g$ as periodic functions of time. The following is a brief description of this procedure.

A Fourier decomposition on the functions $C_l$, $C_d$ and $Nu_g$ gives us

$$C_l = C_{l0} + \sum_{i=1}^{\infty} C_{li} \cdot sin(2\pi it/T_p + \alpha_i), \tag{3}$$

$$C_d = C_{d0} + \sum_{i=1}^{\infty} C_{di} \cdot sin(2\pi it/T_p + \beta_i),$$

$$Nu_g = Nu_0 + \sum_{i=1}^{\infty} Nu_i \cdot sin(2\pi it/T_p + \gamma_i).$$

All coefficients in the Fourier series are positive.

In (3) $C_{l0}$ equals 0; One lets the phase angle of the $C_d$ and the $Nu_g$ series be synchronized by the primary mode of $C_l$. Therefore one can write

$$C_l = C_{l1} \cdot sin(2\pi t/T_p) + HOT,$$

$$C_d = C_{d0} + C_{d1} \cdot sin(2\pi t/T_p + \beta_1) + C_{d2} \cdot sin(4\pi t/T_p + \beta_2) + HOT,$$

$$Nu_g = Nu_0 + Nu_1 \cdot sin(2\pi t/T_p + \gamma_1) + Nu_2 \cdot sin(4\pi t/T_p + \gamma_2) + HOT.$$

The results of $C_{d0}$ and $Nu_0$ (the n=0 mode), $C_{d1}$ and $Nu_1$ (the n=1 mode), $C_{d2}$ and $Nu_2$ (the n=2 mode) are plotted in Figure 7(a) and 7(b) on a semi-log scale. The $C_d$-to-$C_l$ phase lag, $\beta_2$, was shown in Fig. 2.

Physically, the n=0 mode is the time averaged result. Numerically the n=0 mode is temporal error-free, i.e., its value is influenced only by the spatial accuracy of the calculation. The most prominent time dependent behavior for lift is the n=1 mode. For drag and Nusselt number it is the n=2 mode. In fact, geometric constraint prohibits the appearances of n=1

9

mode for the drag coefficient and the global Nusselt number. The $C_{d1}$ and $Nu_1$ therefore represent the dominating numerical errors. From my observation, the magnitudes of $C_{d1}$ and $Nu_1$ reflect primarily the temporal inaccuracy of the calculation. As the CFL number increased as $M_\infty$ decreases, so would the magnitudes of $cd_1$ and $nu_1$ increase. However, by reducing the time step size of integration properly, as was done in the current study on cases of $M_\infty = 0.1$ and $0.2$, the magnitudes of $C_{d1}$ and $Nu_1$ were able to be controlled to a desired level. Behavior of $C_{d1}$ and $Nu_1$ shown in Figure 7 have fully illustrated this argument. Temporal error of the present calculation was controlled at about an order of magnitude smaller than the major time-dependent mode.

$C_{d0}$ versus $M_\infty$ is plotted in Figure 8(a) togather with the measured value from Tritton where $C_{d0} = 1.24$ at $Re_d = 100$ and $M_\infty \sim 0.04$, and from the works of Relf and Wieselsberger where $C_{d0} = 1.36$ as presented in Tritton (1959), and the computational incompressible flow result from Jordan and Fromm of $C_{d0} = 1.28$. When extrapolated to low speed, the current result of $C_{d0} = 1.29$ agrees the best with Jordan and Fromm.

$C_{l1}$ versus $M_\infty$ is plotted in Figure 8(b). A lift coefficients equal to $0.28$ obtained from the present calculation agree more with the value from Jordan and Fromm of $C_{l1} = 0.27$ than with that of $C_{l1} = 0.247$ from Chang and Sa.

$Nu_0$ versus $M_\infty$ is plotted in Figure 8(c). Compared to the result of $Nu_g = 5.23$ evaluated at $Re_d = 100$ using the empirical formula suggested by Eckert and Soehugen (the experimental condition was at $M_\infty \sim 0.02$), and the computational result from Chang and Sa, the current $Nu_0$ of $4.95$ at $M_\infty = 0.1$ is below that value. The reason for this discepancy is believed due to the fact that cylinder was heated in the present simulation, while in the other works the cylinder wall was unheated. The behavior of the $Nu_g$ versus wall heating of a low speed steady flow plotted in Fig. 3(b) illustrates this point. As shown in Fig. 3(b), the computed $Nu_g$ at $(T_w - T_0)/T_w = 0.1$ and $M_\infty = 0.1$ is less than the measured $Nu_g$ of an unheated cylinder by Eckert and Soehugen of about $0.2$. Even though Fig. 3(b) corresponds to the flow condition of $Re_d = 23$.

Strouhal number versus $M_\infty$ is shown in Figure 8(d). Compared to the measured Strouhal

numbers of 0.164 from Tritton and 0.167 from Roshko (1954), the present results with a Strouhal number of about 0.164 are in excellent agreement with those measurements.

Behavior of $C_{d2}$ versus $M_\infty$ can be seen in Fig. 7(a) and Fig. 5 ($C_{d2}$ is approximately half of the tip-to-tip variation of $C_d$ in the phase diagram). At the values of $0.007\pm0.0005$, the current results of $C_{d2}$ are very reasonable when compared to the value of 0.006 obtained by Jordan and Fromm and 0.01 obtained by Chang and Sa.

To illustrate the periodic shedding motion of the current simulation, the vorticity contours for the case of $M_\infty = 0.3$ are shown in Figure 8(e). Four different time frames were plotted. The time increment between each frame was about $T_p/4$.

## 4.3 Vortex Shedding And Breakdown Under Forced Convection

The phenomena of vortex shedding and breakdown under the influence of forced convection were extensively studied by fixing the $Re_d$ at 100, the $M_\infty$ at 0.3, and varing the wall heating ratio, $(T_w - T_0)/T_w$. A total of 10 wall temperature conditions were used, ranging from the mild cooling to the high heating. These cases are $(T_w - T_0)/T_w =$ -0.2, -0.1, 0.1, 0.2, 0.3, 0.4, 0.5, 0.6, 0.75 and 0.9. Gravitational terms were included in the calculations, even though the Groshof numbers defined as

$$Gr = \frac{g(T_w - T_0)(2l)^3}{T_w \nu_\infty^2},$$

were no greater than $2\times10^{-4}$ in this work. This means the gravitational effect was actually negligible in comparison to the effect of advection, viscous diffusion, and dissipation.

The initial temperature field was given an exponentially decaying profile from the cylinder wall to the outer boundary. Simulation was stopped after the limit cycle had been well established for flows with periodic shedding or after the symmetrical flow patterns were stabilized for steady flows.

Periodic vortex shedding was observed at all mild cooling and heating situations, that is for $(T_w - T_0)/T_w$ less than 0.6. For $(T_w - T_0)/T_w \geq 0.6$, steady flows with twin trailing vortices occurred. The lift coefficient-to-drag coefficient ($C_l$-$C_d$) phase diagrams of cases with

11

periodic shedding are shown in Figure 9. The time dependent behavior of the global Nusselt numbers ($Nu_g$) are plotted in Figure 10.

As before, the FFT analysis was performed on $C_l$, $C_d$ and $Nu_g$. The n=0 modes, n=1 modes and n=2 modes of the decomposed $C_d$ and $Nu_g$ are shown in Figure 11(a) and 11(b) respectively on a semi-log scale. The physical time step sizes used in this work were carefully chosen. A $\Delta t = 0.04$ was used for cases when $(T_w - T_0)/T_w$ = -0.2, -0.1, 0.1 and 0.2. $\Delta t = 0.03$ was used when $(T_w - T_0)/T_w = 0.3$ and 0.4. And $\Delta t = 0.02$ was used when $(T_w - T_0)/T_w$ = 0.5 and 0.6. As a result, the leading errors, $C_{d1}$ and $Nu_1$, were about four times smaller than the major time dependent modes $C_{d2}$ and $Nu_2$, as is indicated in Fig. 11. Naturally the smaller the $C_{d1}$ and $Nu_1$ the better. If one's prime interest were to analyze the influence of the next highest modes, the n=4 modes of $C_d$ and $Nu_g$, on the flow, then one should make sure $C_{d1}$ and $Nu_1$ do not overwhelm $C_{d4}$ and $Nu_4$. This can be done by further reducing the time step size. In the present study, we do not feel the next highest modes can have impact on the vortex breakdown phenomenon. The current level of temporal accuracy was considered acceptable.

Figure 12 shows the behavior of $C_{l1}$, the n=1 mode of the lift coefficient, versus wall heating ratio. $C_{l1}$ is seen to decrease sharply to zero at about $(T_w - T_0)/T_w = 0.6$ and remains zero from that point on. Obviously, it indicates that when $(T_w - T_0)/T_w$ is less than 0.6, periodic shedding occurs. When $(T_w - T_0)/T_w \geq 0.6$, the shedding stops. This sudden termination of the vortex shedding can be seen clearly by examining the behavior of Strouhal number (S) shown in Figure 13. When $(T_w - T_0)/T_w$ is less than 0.6, S exhibits a finite magnitude. When $(T_w - T_0)/T_w \geq 0.6$, S is zero. The finite jump of S at $(T_w - T_0)/T_w \sim 0.6$ represents the existence of a preferred frequency for a blunt body. That periodic shedding, if it occurs, can become self-sustaining only at a certain frequency.

What deserves attention is the monotonically decreasing trend of the Strouhal number with respect to wall heating obtained in the current study. It is distinctively different from the experimental observation of Noto et al. and from the numerical results of Chang et al. for an incompressible buoyancy dominated flow. In these works the Strouhal numbers

12

showed a rising trend with respect to wall heating. At some point before the wall temperature became high enough to make shedding disappear, the Strouhal number started to turn sharply downward (Chang's sample was not large enough to tell whether or not the downward trend existed in the mathematical model for incompressible flow). The current results show Strouhal number decreases monotonically but slowly in the mild cooling and heating region, that is $(T_w - T_0)/T_w$ between -0.2 and 0.2. As the heating increases, S goes downward with seemingly a larger and larger negative slope. The decreasing trend of S is physically reasonable. It represents the slow down of the emission of vortex before it can come to a stop. The increasing trend of S with respect to heating shown by Noto and by Chang represented an increase in the vortex emission. This tendency is against the final outcome of the physical process because emission of the vortex eventually stops at a higher heating ratio. It could happen only if buoyancy provided a destabilizing effect at the beginning. When wall heating reached a certain level, this destabilizing effect suddenly changed its characteristics and turned into a stabilizing effect. It is a rather complicated physical process. From the results presented by Chang and Sa, this must be what have happened with the incompressible mathematical model. Since in our work buoyancy is negligibly small, it is very reasonable for Strouhal number to decrease monotonically with respect to wall heating under the simple argument that wall heating provides only a stabilizing effect to the global instability in the present study. As to what the stabilizing effect might be and what its relation are to the wall heating will be explained in the next section.

Another distinctively different trend is the behavior of the global Nusselt number ($Nu_g$) with respect to wall heating. The results of Chang and Sa show $Nu_g$ increased with respect to the increase in wall temperature in the cooling zone (i.e., in the region where $T_w$ was less than $T_0$). Then $Nu_g$ showed a decreasing trend in the heating zone untill it reached a local minimum at the wall temperature where vortex shedding stopped. After that, the $Nu_g$ turned sharply back to the growing trend again. The present results differ from those of Chang and Sa. In this work $Nu_g$ decreases monotonically with respect to wall heating as shown in Figure 14. At the jump point, i.e., at $(T_w - T_0)/T_w \sim 0.6$ the point where shedding stops, $Nu_g$ shows

13

no sign of discontinuity at all. After the jump point, $Nu_g$ continues to go down with the same slope as before. The monotonically decreasing trend of $Nu_g$ here, particularly in the steady flow region, is consistent with the behavior of $Nu_g$ shown by the baseline test cases presented earlier (see Section 4.1). The reason for not having a discontinuity at the jump point is largely due to the fact that not only $Nu_g$ decreases both before and after the jump point but $Nu_g$ also exhibits less and less time dependency (see Fig. 10 and Fig. 11) as the wall temperature increases. At $(T_w - T_0)/T_w$=0.5, $Nu_g$ is virtually time independent. It blends smoothly into the steady flow's behavior across the jump point without showing a discontinuity.

The $Nu_g$ increased monotonically with respect to wall heating in the steady flow region in Chang's results must be the fact that their mathematical formulation was for incompressible flows. This does not allow local density variation to occur. The viscous boundary layer could not expand under wall heating and the thermal layer turned sharper and sharper. Therefore $Nu_g$ became higher for the higher wall temperature gradient in their calculation. The present model is for compressible flows. Under the same static pressure field the density is inversely proportional to the local temperature. This allows the viscous layer and thermal layer to expand with respect to wall heating. The local variation of density is significant in this work. $Nu_g$ behaves differently under the present model as opposed to that under Chang's model as expected.

The behavior of drag coefficient ($C_{d0}$) in the present study is consistent with the trend shown by Chang and Sa. In Figure 15, $C_{d0}$ shows a slowly increasing trend in the shedding zone with respect to wall heating. It turns to a sharper growing slope in the steady flow region. The reason drag grows faster when shedding stops is due to the fact that steady twin vortices flows have innately stronger form drag than the flows with periodic shedding. Form drag grows fast when the boundary seperation points move back toward the trailing edge point. Boundary seperation points moved particularly fast in the steady flow region with respect to wall heating in the present calculations. Therefore, the $C_{d0}$ took on a much larger growing slope after the shedding had stopped. The locations of the seperation points for all

14

cases calculated in the wall heating zone are listed in Table I for reference.

Through out the course of this article, the author have stressed that the buoyancy effect is inconsequential to the current event. To verify this, cases of $(T_w - T_0)/T_w = 0.4, 0.5$ and $0.6$, which cover the neighborhood of the turning point of the flow structure, were calculated over again without the gravitational terms in the governing equations. Results from these calculations showed no meaningful difference from the previously obtained values.

## 5. CONCLUDING REMARKS

Qantitatively I have shown the contrast between the buoyancy dominated vortex break-down studied by Noto et al. and by Chang et al. , and the present study which disappearing of the vortex street has occurred in a convection dominated compressible flow with negligibly small buoyancy effect. It is clear that reasons described by Noto et al. and by Chang et al. to be the cause of the vortex breakdown in their works do not characterize the breakdown in the present study.

In the previous section, I have argued that wall heating provides only a stabilizing effect on global instability in this study. Here I will further argue that this stabilizing effect comes from the fact that the near wall effective Reynolds number has been reduced by wall heating through convection and comprssibility of the flow.

In supporting to these arguments, flow patterns for the selective cases of $(T_w - T_0)/T_w = -0.2, 0.2, 0.5, 0.6, 0.75$ and $0.9$ were plotted. The first three cases provide a look at flows with periodic shedding. The last three provide a look at steady flows, with proper incremental increase on the wall heating. Figure 16 shows the streamline contours. Normalized stream function from -0.1 to 0.1, with an increment of 0.01 are shown. The growth of the viscous boundary layers, indicated by the expansion of the near wall contours, can be seen. Figure 17 shows the isothermal contours with 31 levels of normalized temperature. The expansion of the near wall contours represents the growth of the thermal layers. The elongated shedding contours in the wake, as the heating increases, indicate the weakened intensity of

15

the perturbed temperature field (excluding the time-averaged flow field). Figure 18 shows the contours of the vorticity magnitude. The elongated attached shedding vortices at higher heating ratio demonstrate the slow down of the vortex emission and the weakening of the perturbed velocity field due to wall heating.

These figures are the qualitative proofs for the argument that wall heating stabilizes the flow. Quantitative evidence is shown in Figure 19, where the time-averaged centerline velocity $(U_c/U_\infty)$ at the near wake for cases of $(T_w - T_0)/T_w = $ -0.1, 0.2 and 0.5 are shown. Contrasted to the measurements made by Noto et al., in which the time averaged centerline velocity in the wake was pulled by the buoyant force as the temperature increased, the results of $U_c$ in this work have actually decreased significantly with respect to wall heating. Also, from the fact that the time averaged density, $(\rho_c/\rho_\infty)$, decreased as the heating increases (see Figure 20), I have come to the conclusion that the breakdown of the vortex street in the present study is due to the effective flow Reynolds number in the near wall and the near wake regions being reduced by the heating of the wall through flow convection and compressibility. As a result, when $(T_w - T_0)/T_w$ becomes larger, the flow pattern more and more resembles a lower Reynolds number flow. That is why as the wall temperature increased, the boundary layers became thicker, the flow seperation points moved downstream, the drag increased, and the Nusselt number and Strouhal number decreased. Finally, when the amount of wall heating was high enough, a state was reached in which the perturbed flow field had lost all its energy and vanished.

# REFERENCES

Borthwick, A. 1986 *Intl J. Num. Meth. Fluids* **6**, 275.

Chang, K. and Sa, J. 1990 *J. Fluid Mech.* **220**, 253.

Chen, S., Liu, N. and Kim, H. 1991 *NASA TM-105259* (submitted to *J. comp. phys.*)

Eckert, E. R. G. and Soehngen, E. 1952 *Trans. ASME* **74**, 343.

Jordan, S. K. and Fromm, J. E. 1972 *Phys. Fluids* **15**, 371.

Noto, K., Ishida, H. and Matsumoto, R. 1985 *Flow Visulization III.* , 348. Springer.

Roshko, A. 1954 *Rep. Nat. Adv. Comm. Aero., Wash.*, no. **1191**.

Tritton, D. J. 1959 *J. Fluid Mech.* **6**, 547.

| $(T_w - T_0)/T_w$ | Seperation Pts. (deg.) |
|---|---|
| 0.1 | $(\pm)$ 61.0 $\pm$ 2.75 |
| 0.2 | $(\pm)$ 60.3 $\pm$ 2.3 |
| 0.3 | $(\pm)$ 59.2 $\pm$ 1.6 |
| 0.4 | $(\pm)$ 58.0 $\pm$ 1.0 |
| 0.5 | $(\pm)$ 56.4 $\pm$ 0.6 |
| 0.6 | $(\pm)$ 54.1 |
| 0.75 | $(\pm)$ 47.5 |
| 0.9 | $(\pm)$ 28.4 |

Table I. Location of seperation points. $Re_d$=100, $M_\infty$=0.3.
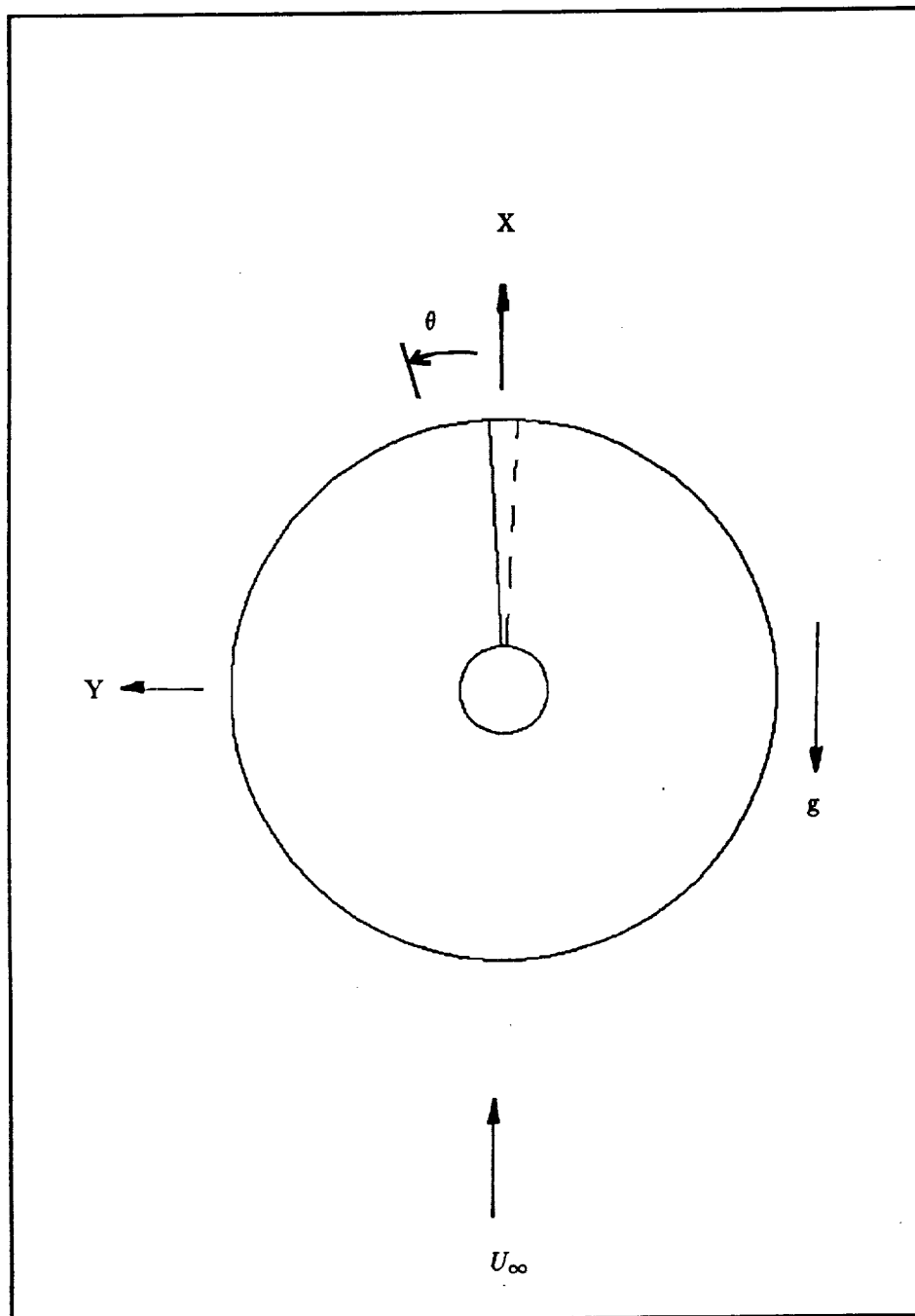
Figure 1. Schematic representation of flow domain used.
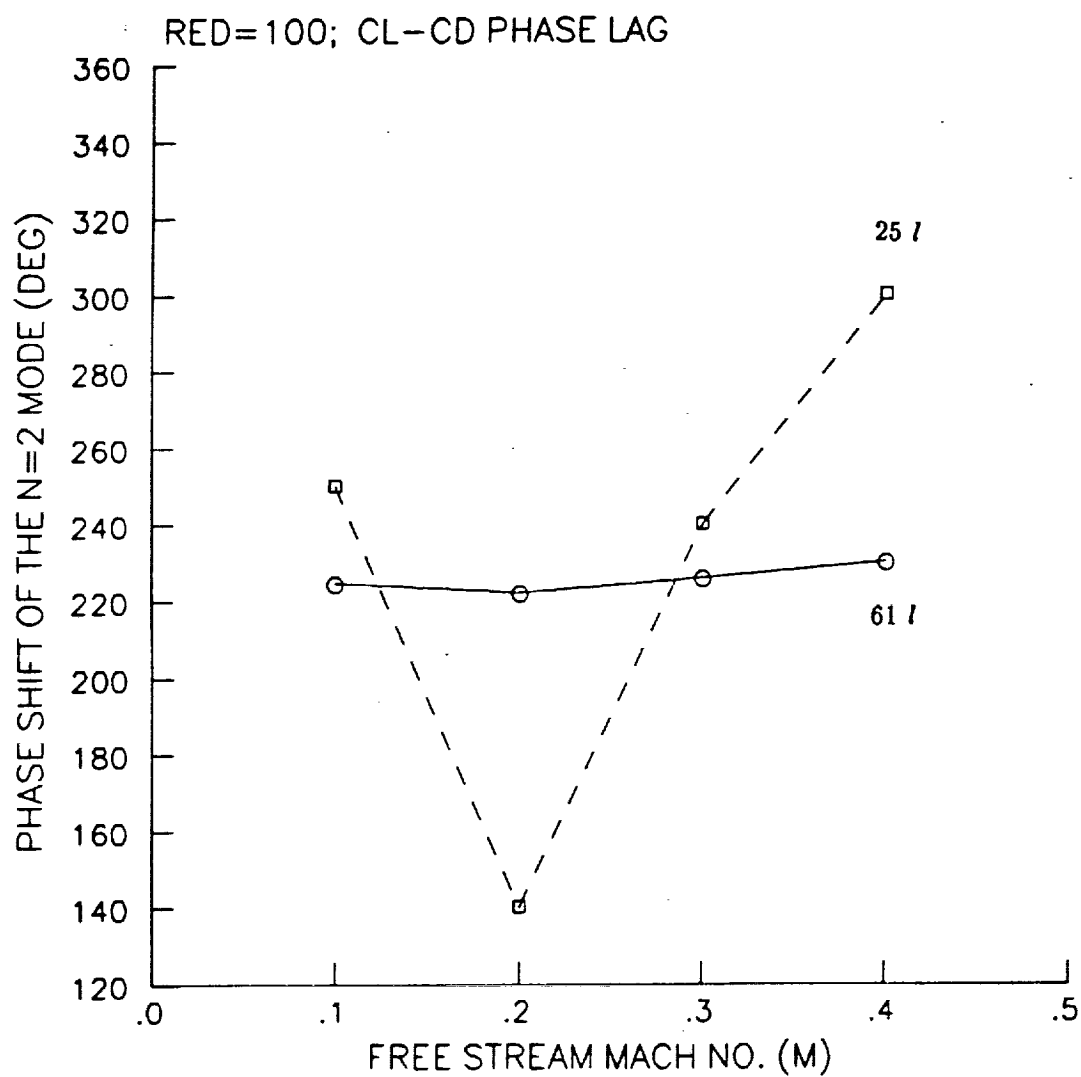
Figure 2. Influence of the outer radius on the phase lag of $C_d$-$C_l$.

(a)



(b)



(c)
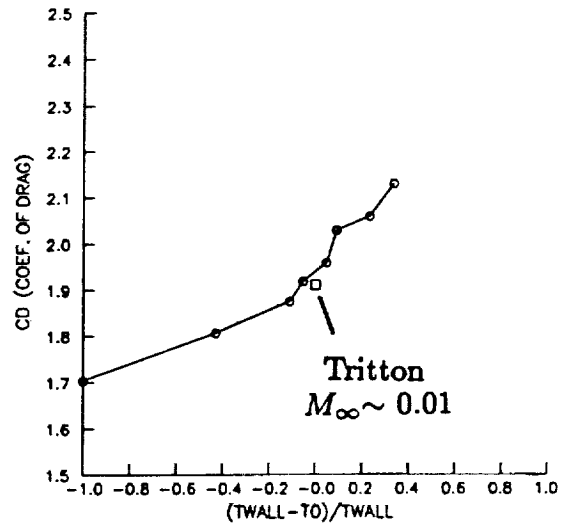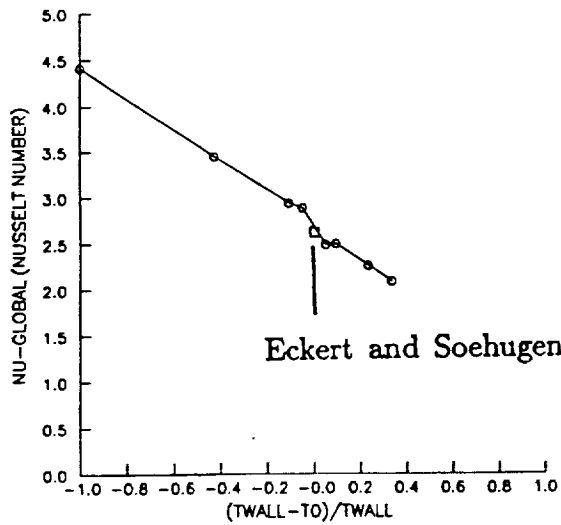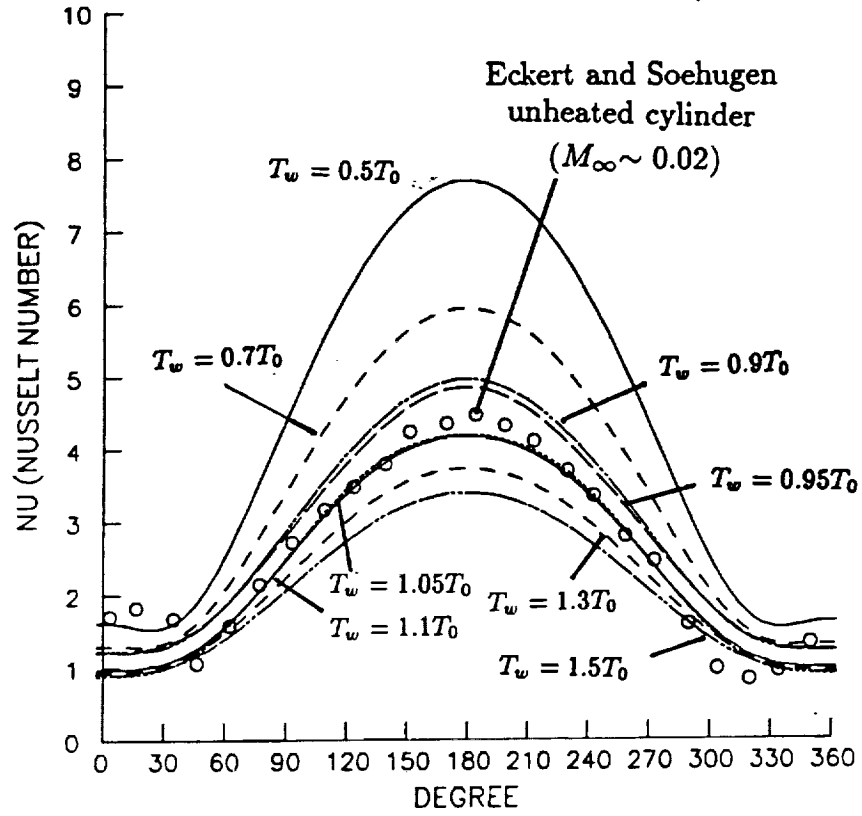
Figure 3. (a). Local Nusselt number vs. $(T_w - T_0)/T_w$, (b). Global Nusselt number vs. $(T_w - T_0)/T_w$, (c). $C_d$ vs. $(T_w - T_0)/T_w$. $Re_d$=23, $M_\infty$=0.1.

21

$$T_w = 0.9T_0$$



$$T_w = 1.1T_0$$

Figure 4. Isothermal contours of $T_w=0.9T_0$ and $T_w=1.1T_0$ . $Re_d=23$, $M_\infty=0.1$.

SHEDDING/RED=100 M=0.1, DT/TW=0.1

SHEDDING/RED=100 M=0.2, DT/TW=0.1

SHEDDING/RED=100 M=0.3, DT/TW=0.1

SHEDDING/RED=100 M=0.4, DT/TW=0.1
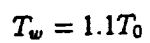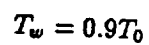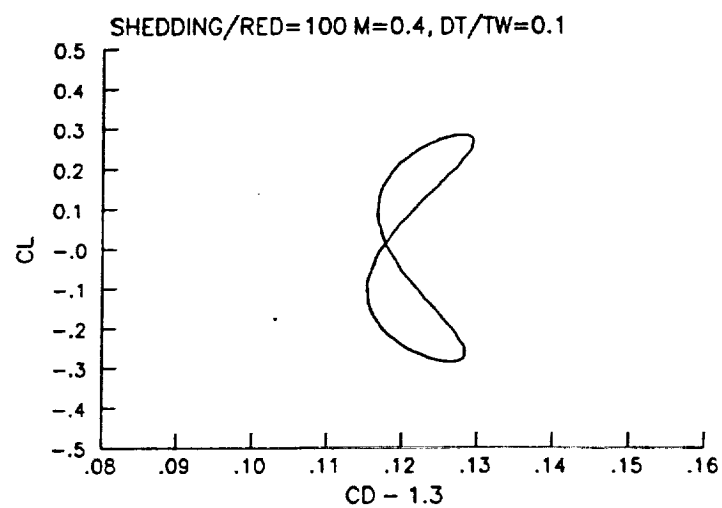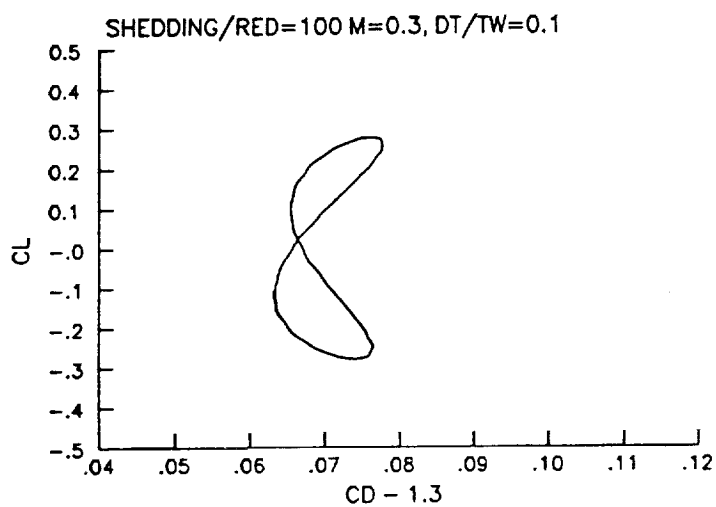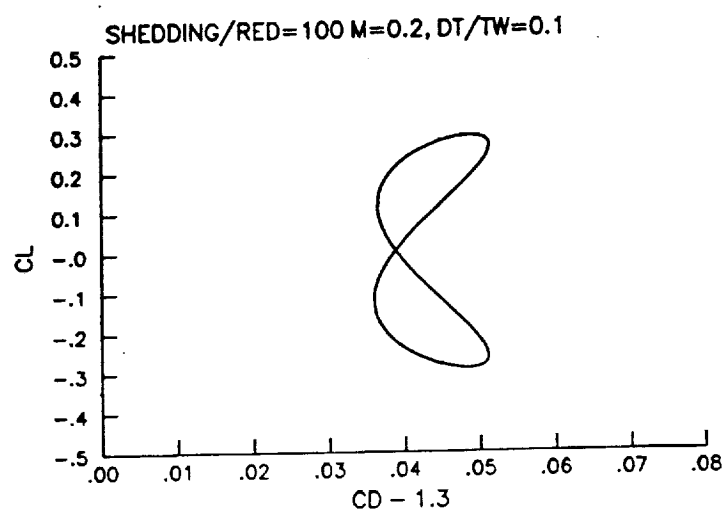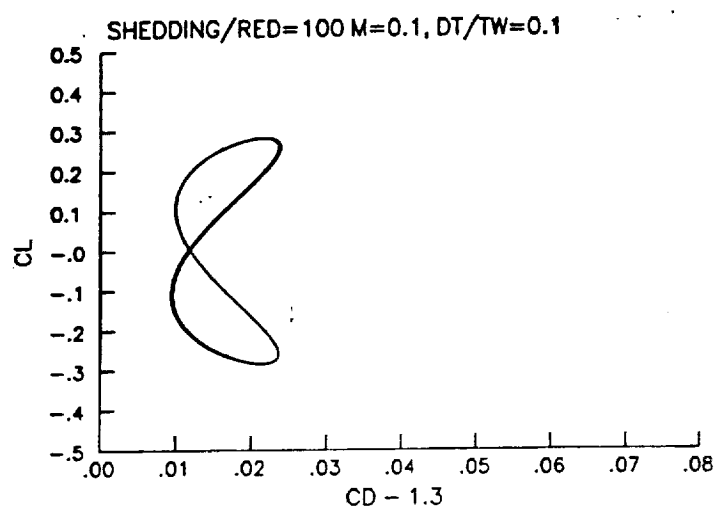
Figure 5. $C_l$-$C_d$ phase diagram under various $M_\infty$. $Re_d$=100, $(T_w - T_0)/T_w$=0.1.
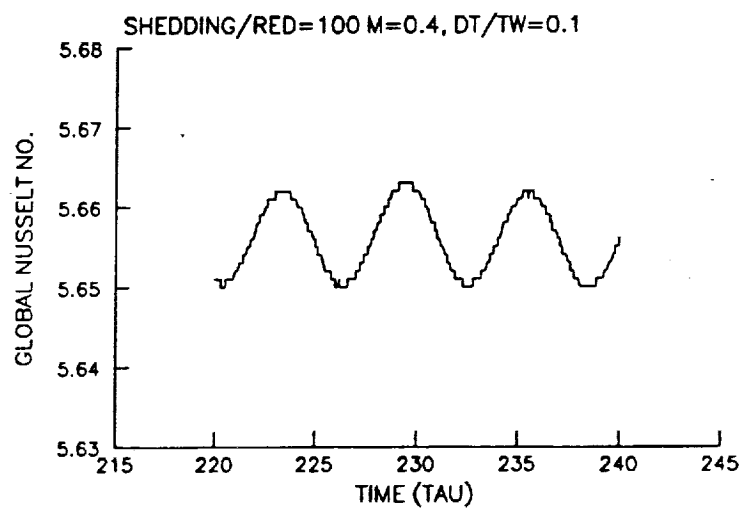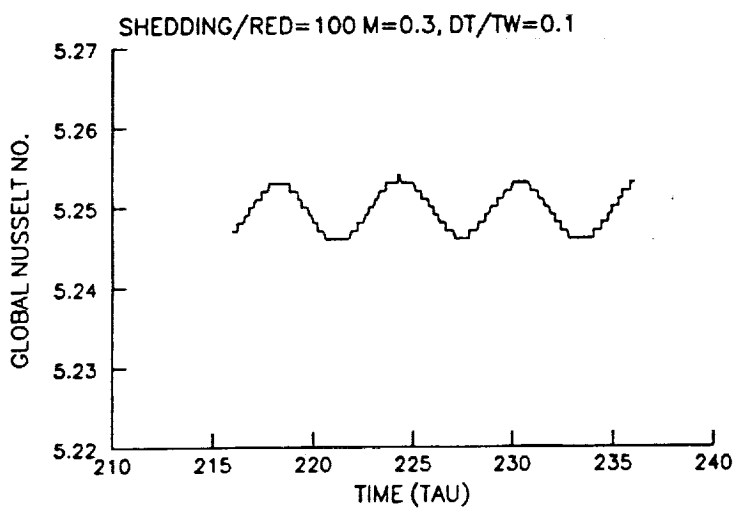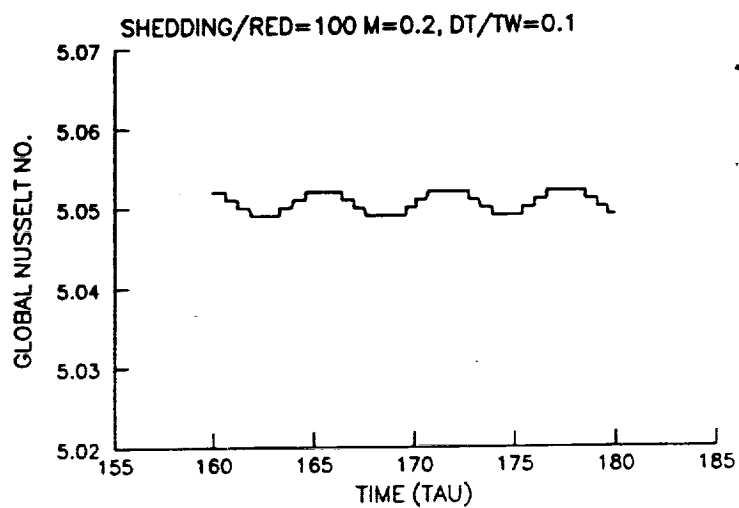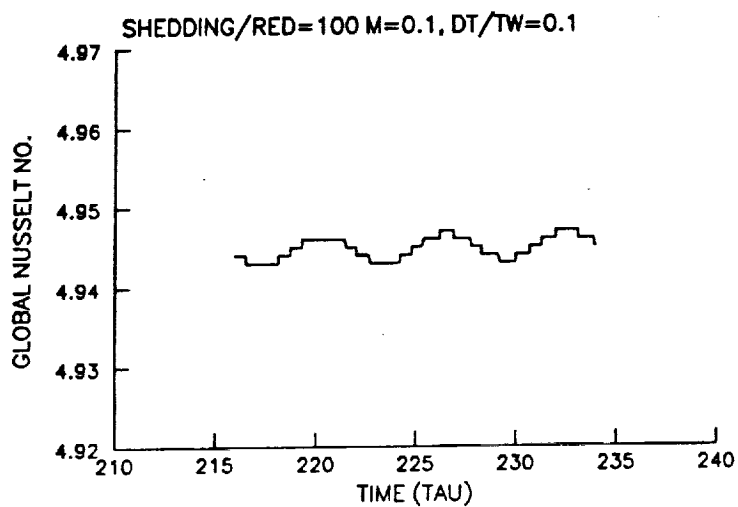
Figure 6. $Nu_g$ vs. time under various $M_\infty$. $Re_d$=100, $(T_w - T_0)/T_w$=0.1.
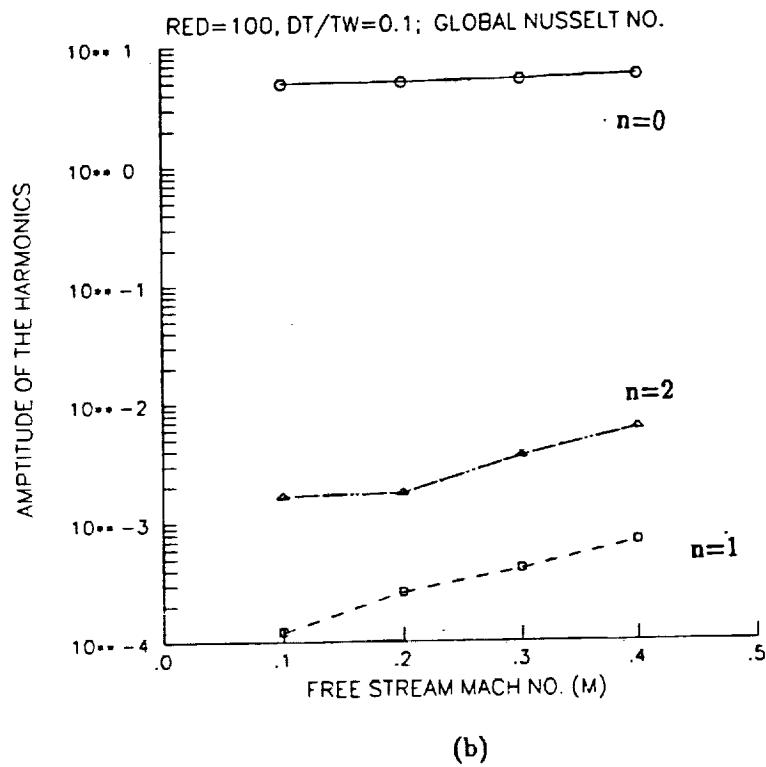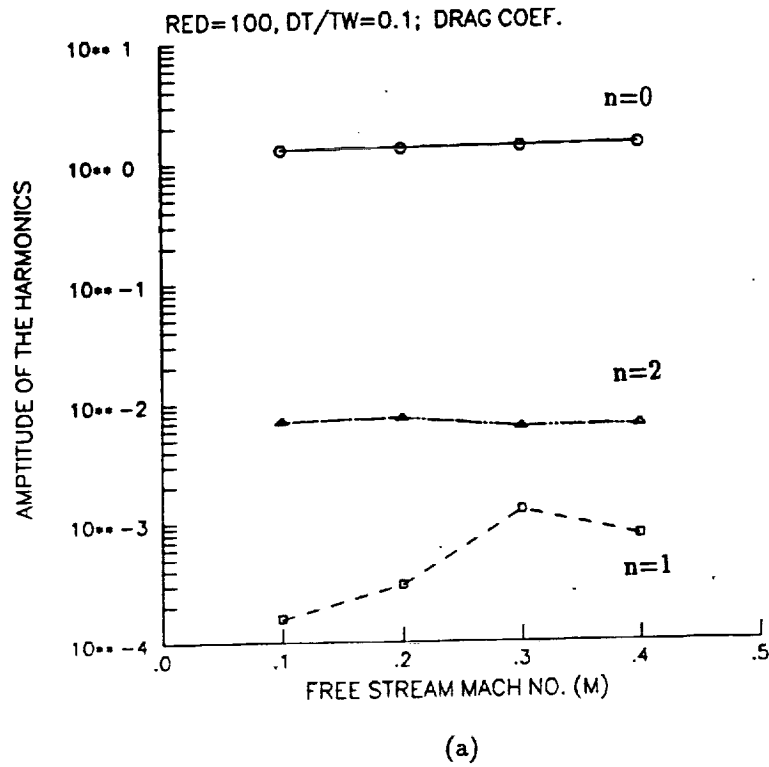
Figure 7. Amptitude of the modes: (a). $C_d$ vs. $M_\infty$, (b). $Nu_g$ vs. $M_\infty$. $Re_d$=100, $(T_w - T_0)/T_w$=0.1.

25
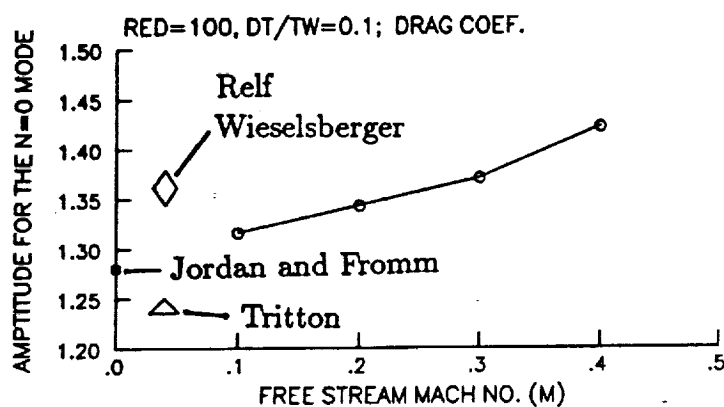
**(a)**
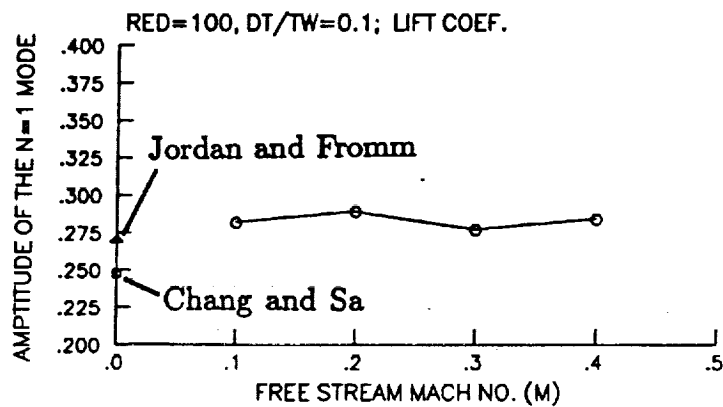
**(b)**
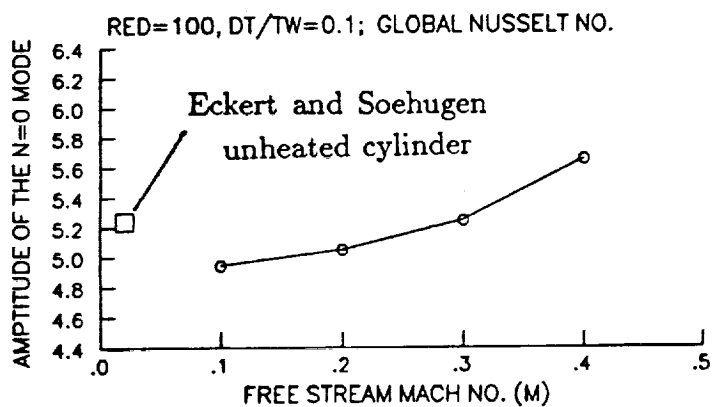
**(c)**
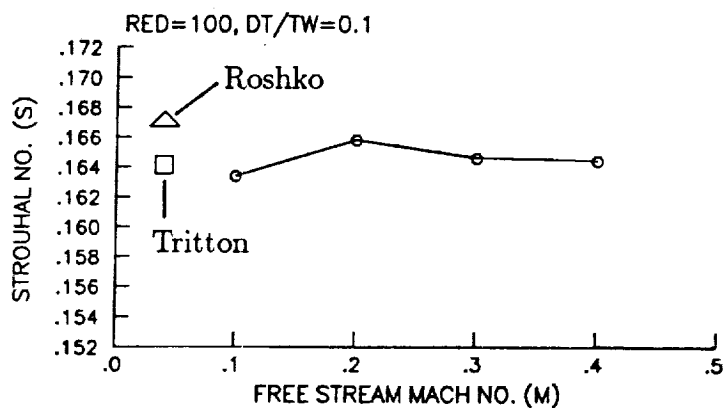
**(d)**

Figure 8. At $Re_d=100$, $(T_w - T_0)/T_w=0.1$: (a). $C_{d0}$ vs. $M_\infty$, (b). $C_{l1}$ vs. $M_\infty$, (c). $Nu_0$ vs. $M_\infty$ and (d). Strouhal number vs. $M_\infty$.
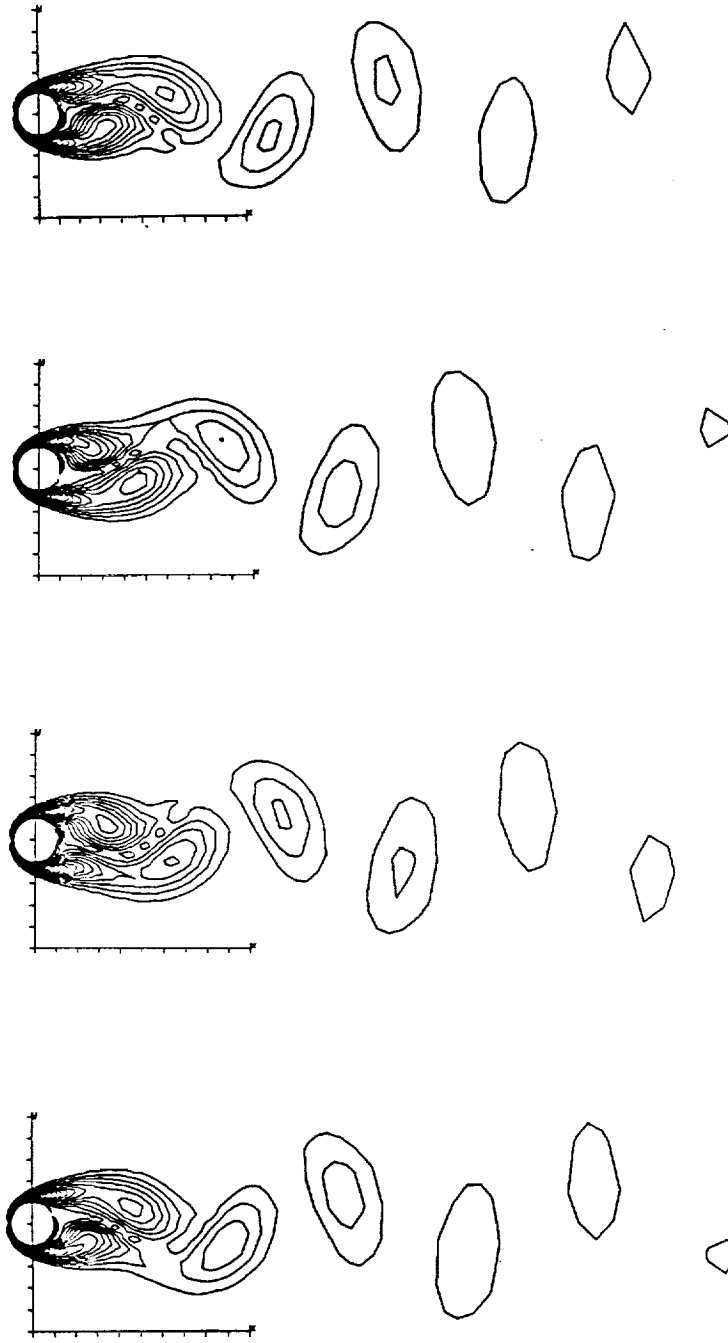
Figure 8. (e). Contours of vorticity magnitude for the case of $M_\infty=0.3$. $Re_d=100$, $(T_w - T_0)/T_w=0.1$.
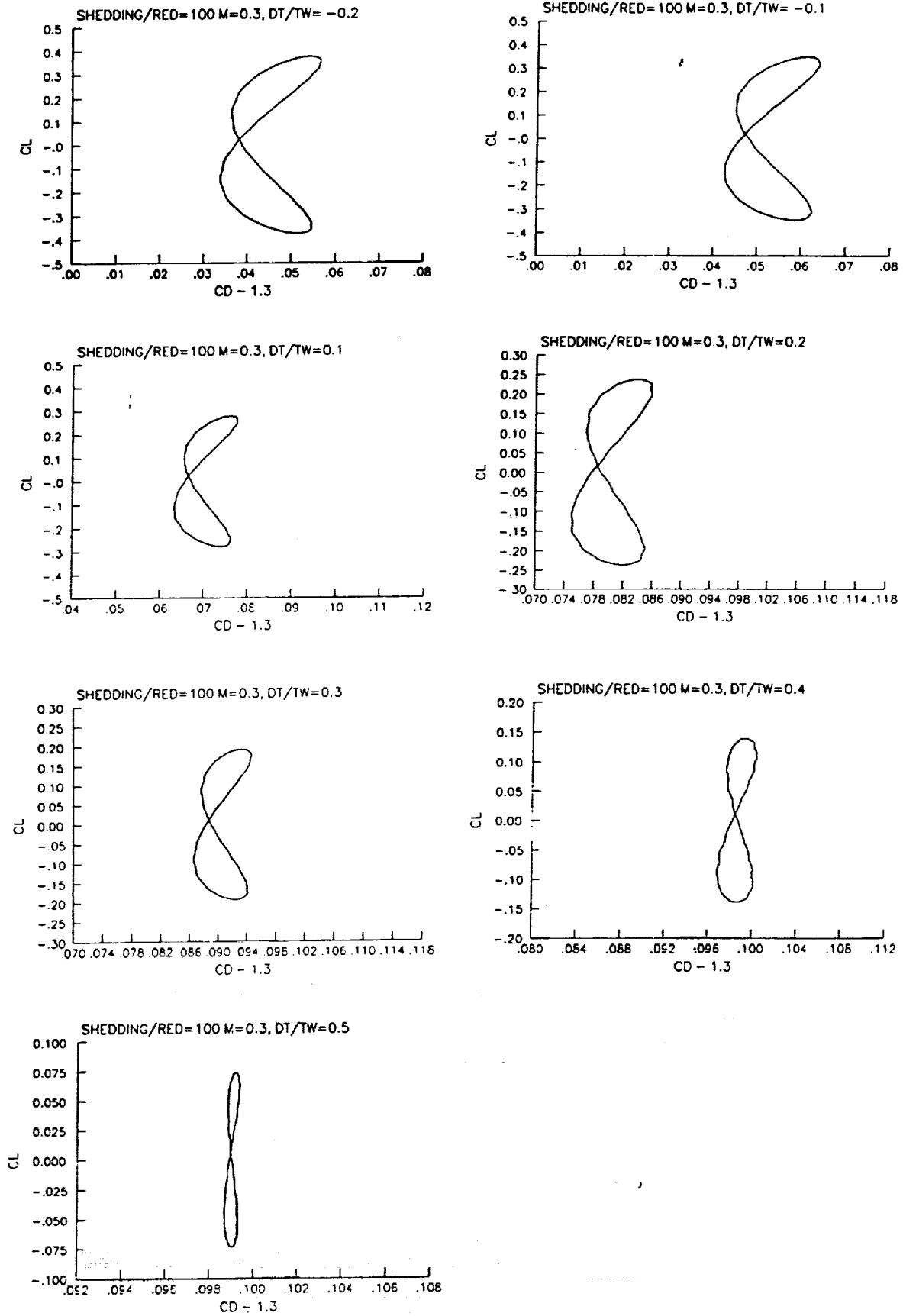
Figure 9. $C_l$-$C_d$ phase diagram at various wall temperature. $Re_d=100$, $M_\infty=0.3$.
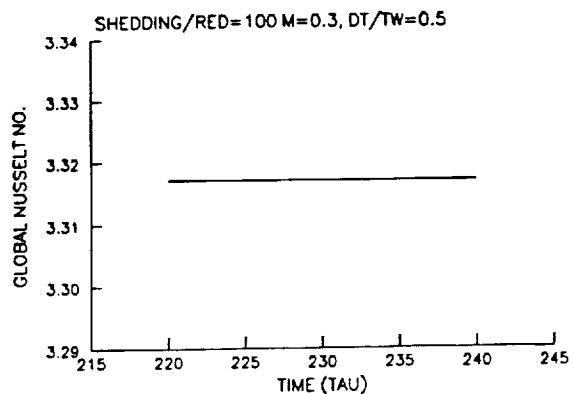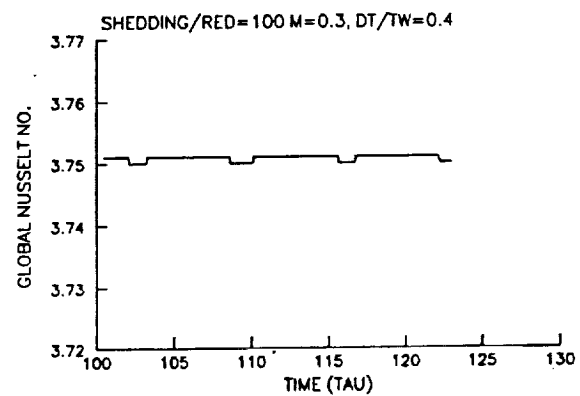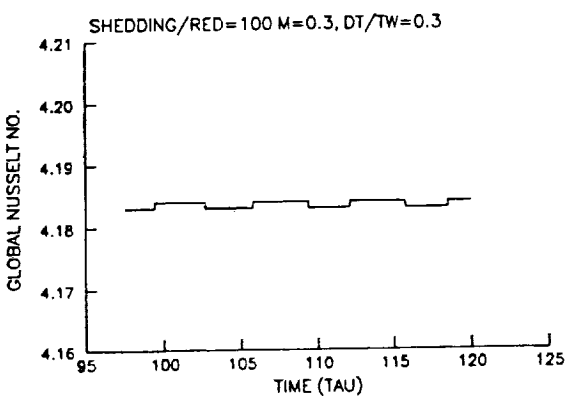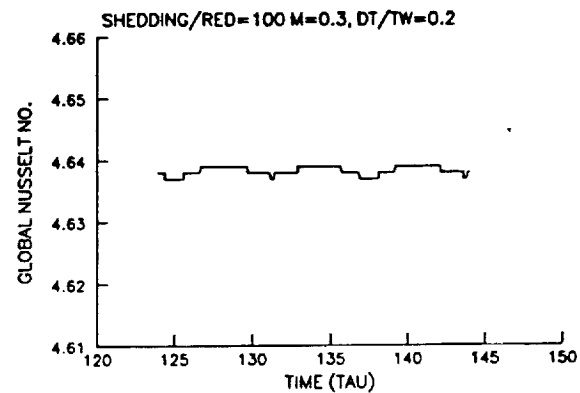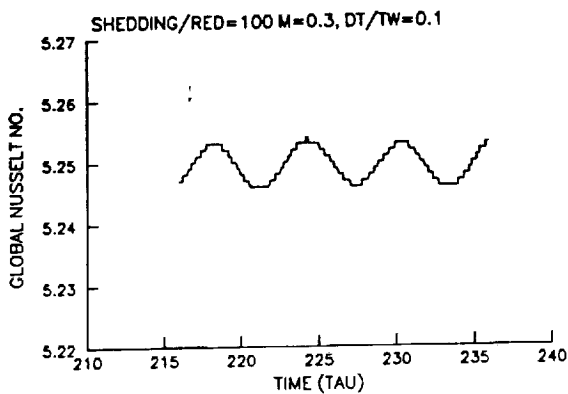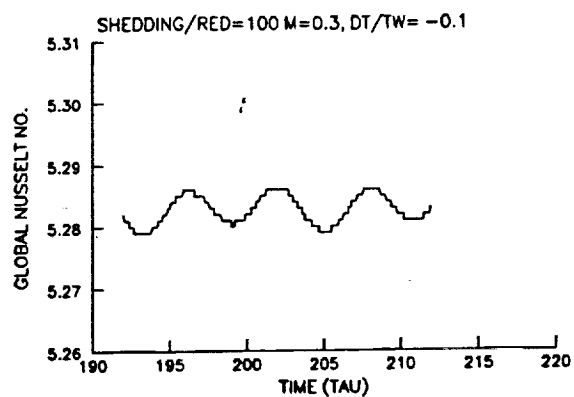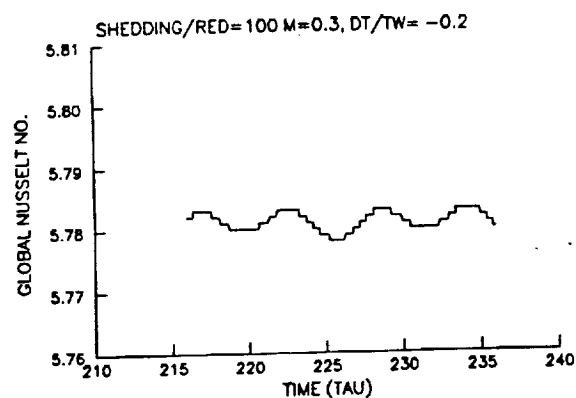
Figure 10. $Nu_g$ vs. time at various wall temperature. $Re_d=100$, $M_\infty=0.3$.

29

(a)



(b)
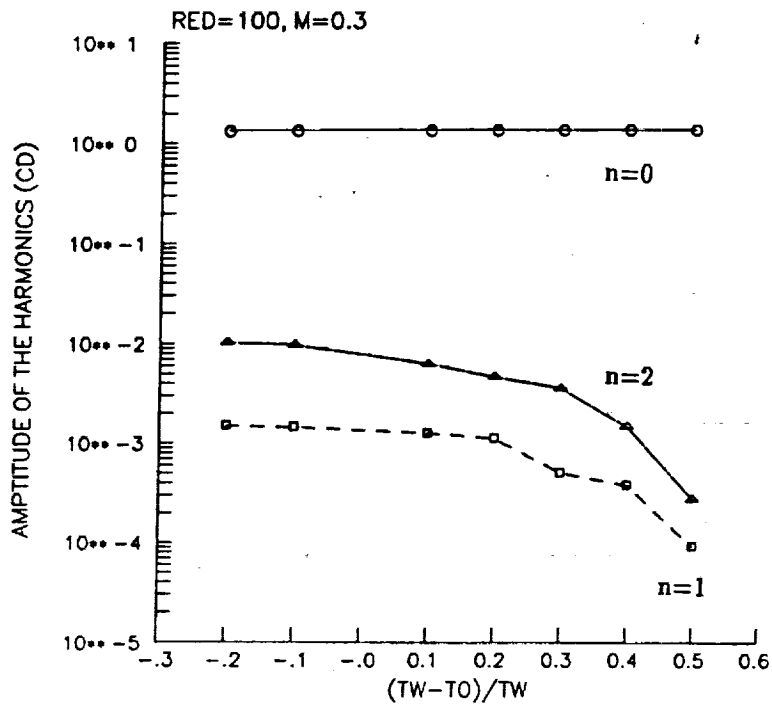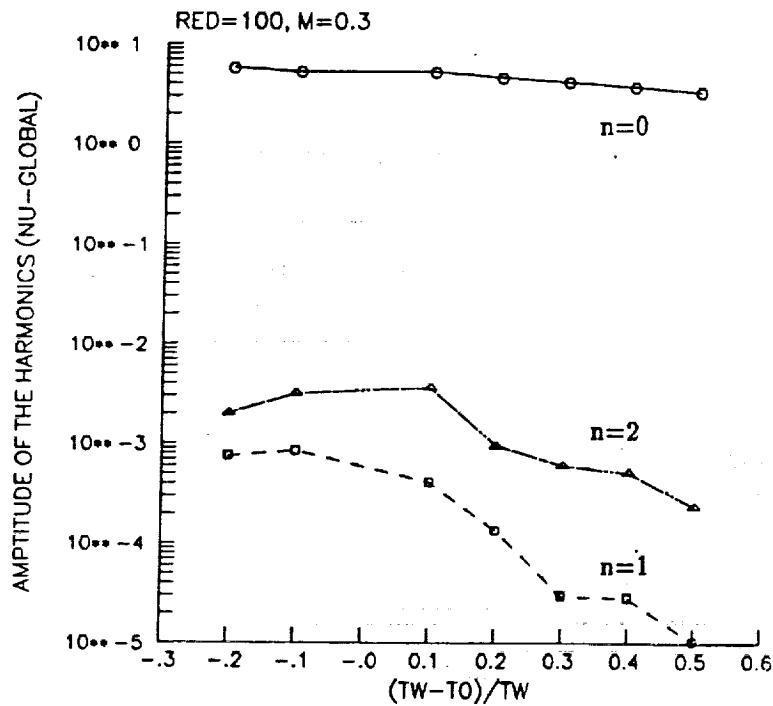
Figure 11. Amptitude of the modes: (a). $C_d$ vs. $(T_w - T_0)/T_w$, (b). $Nu_g$ vs. $(T_w - T_0)/T_w$. $Re_d$=100, $M_\infty$=0.3.
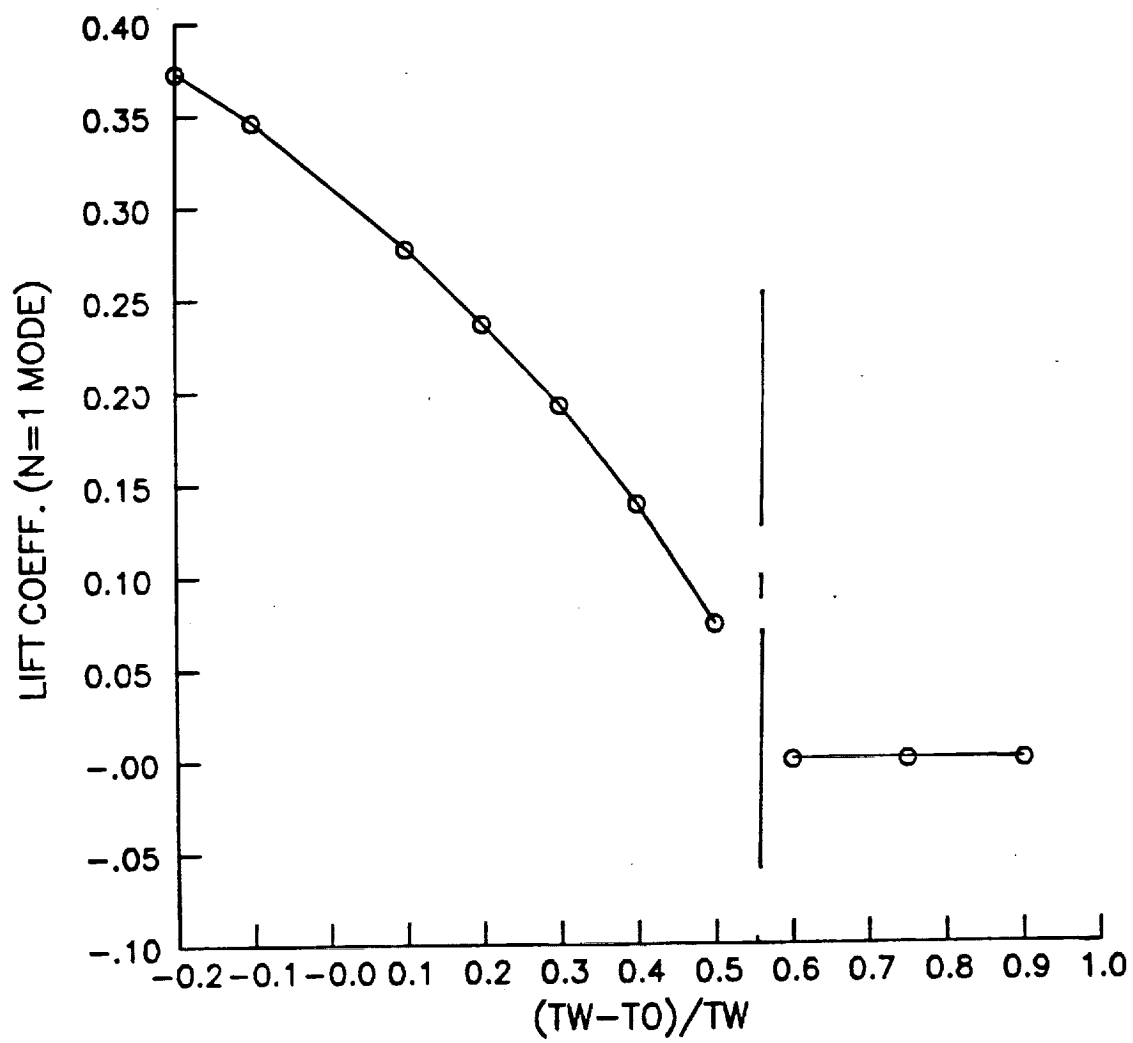
Figure 12. $C_{l1}$ vs. $(T_w - T_0)/T_w$. $Re_d$=100, $M_\infty$=0.3.
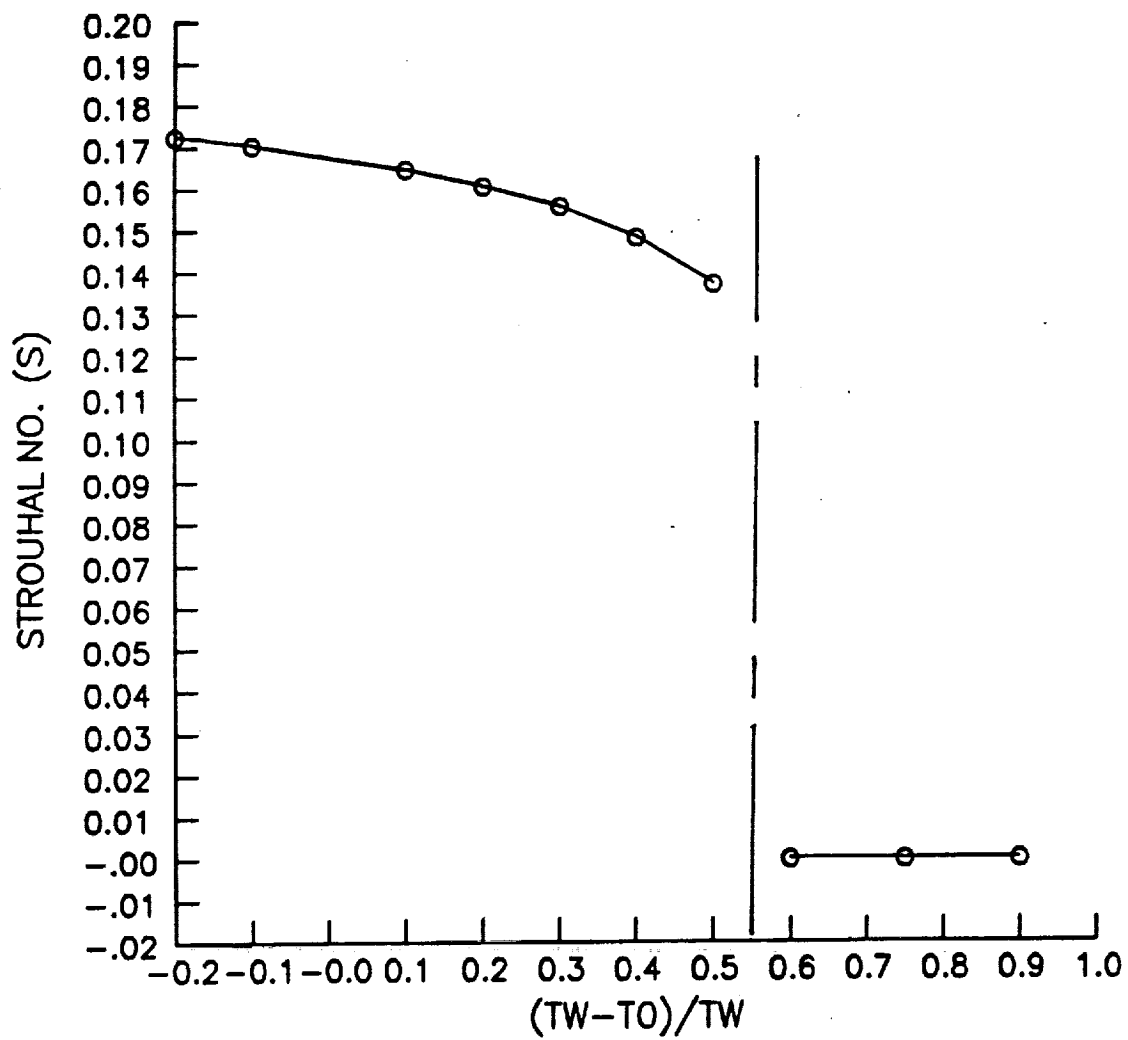
Figure 13. Strouhal number vs. $(T_w - T_0)/T_w$. $Re_d=100$, $M_\infty=0.3$.
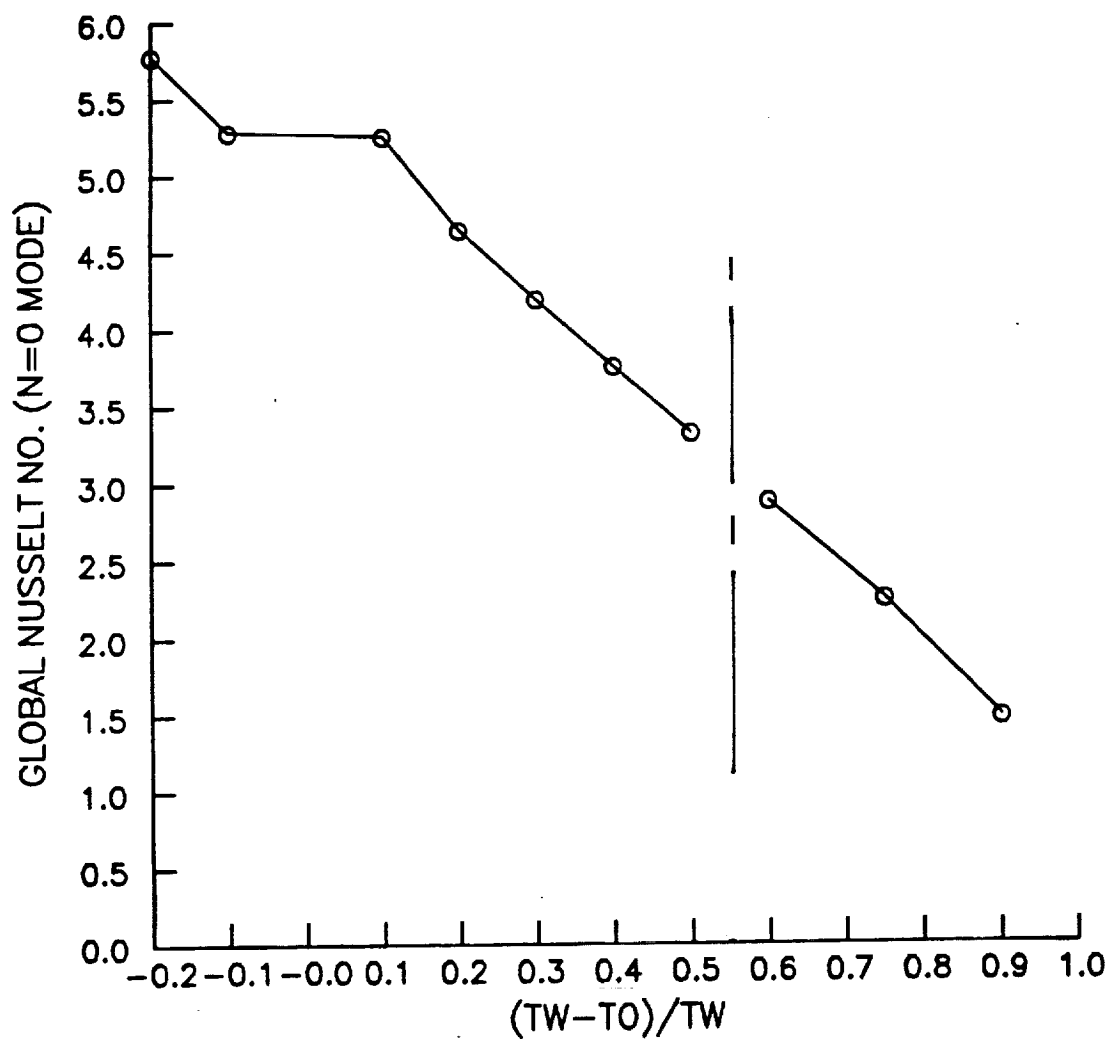
Figure 14. Global Nusselt number vs. $(T_w - T_0)/T_w$. $Re_d$=100, $M_\infty$=0.3.
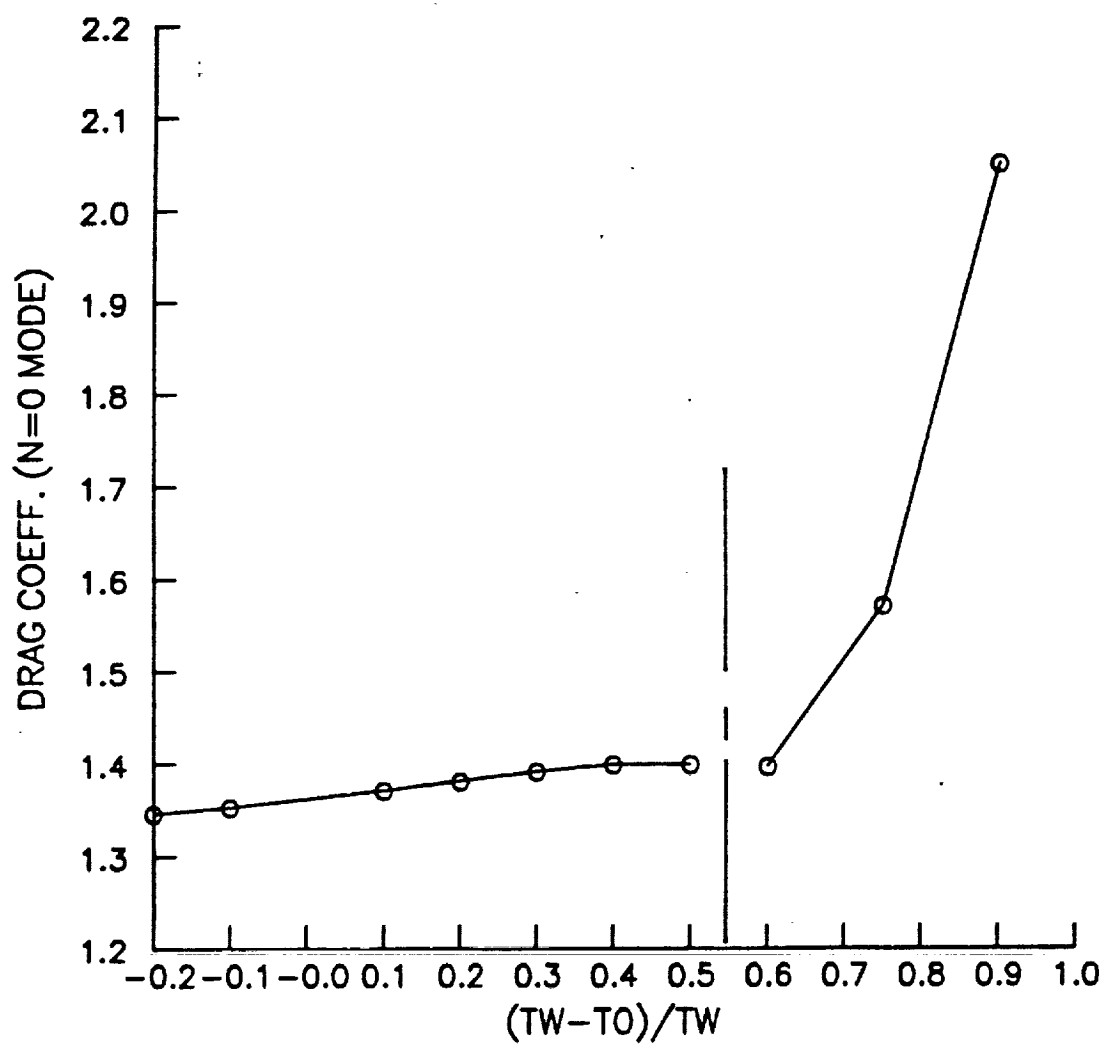
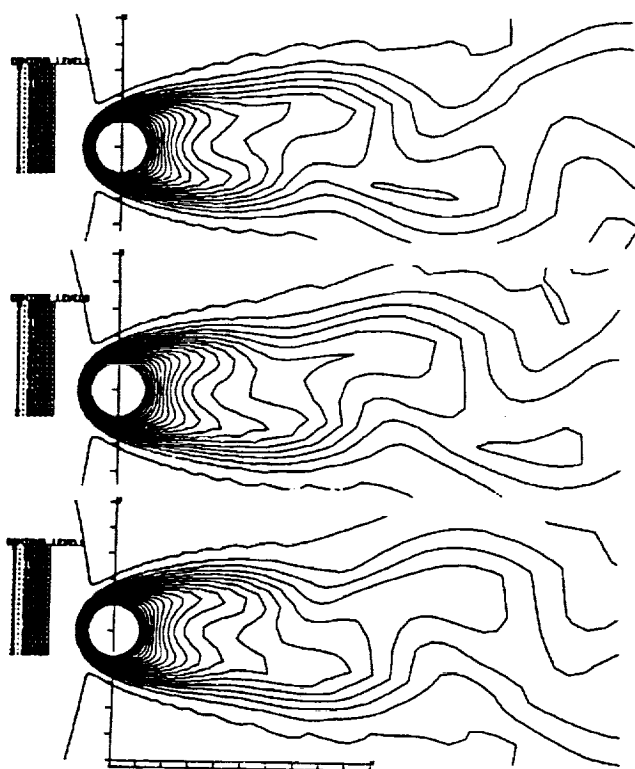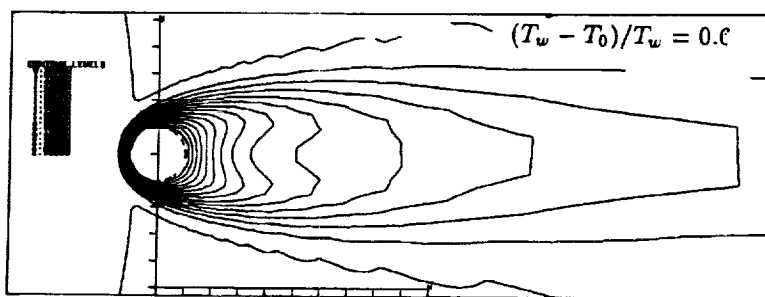Figure 15. Time averaged drag coefficient vs. $(T_w - T_0)/T_w$. $Re_d$=100, $M_\infty$=0.3.

$(T_w - T_0)/T_w = -0.2$

$(T_w - T_0)/T_w = 0.2$

$(T_w - T_0)/T_w = 0.6$

$(T_w - T_0)/T_w = 0.75$
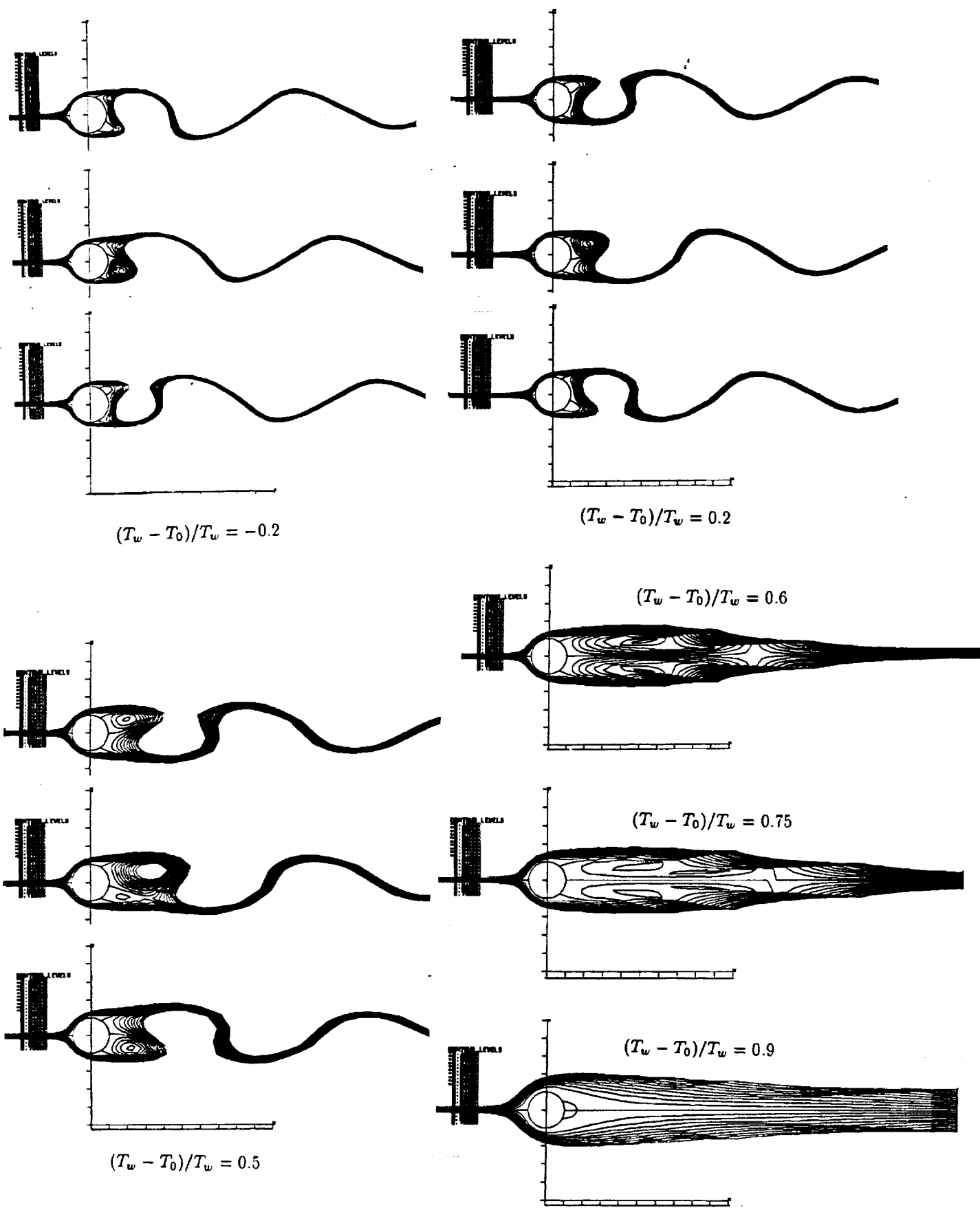
$(T_w - T_0)/T_w = 0.9$

$(T_w - T_0)/T_w = 0.5$

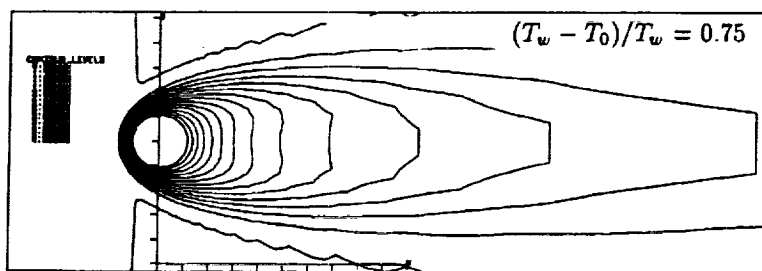Figure 16. Streamline contours. $Re_d$=100, $M_\infty$=0.3.
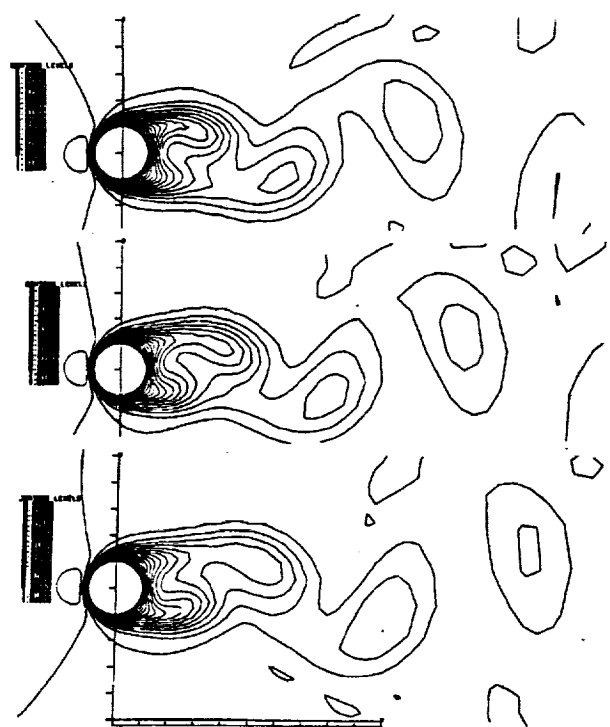
$(T_w - T_0)/T_w = -0.2$
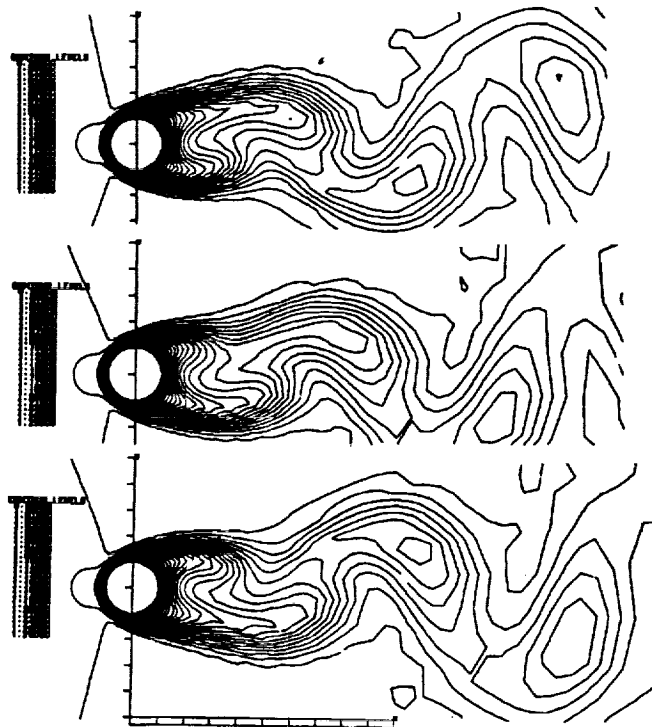
$(T_w - T_0)/T_w = 0.2$
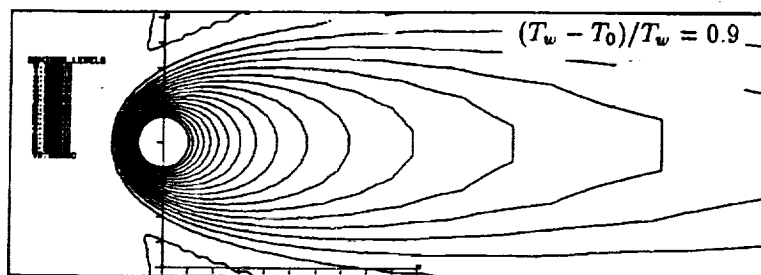
$(T_w - T_0)/T_w = 0.0$

$(T_w - T_0)/T_w = 0.75$

$(T_w - T_0)/T_w = 0.9$

$(T_w - T_0)/T_w = 0.5$

Figure 17. Isothermal contours. $Re_d$=100, $M_\infty$=0.3.

36

$(T_w - T_0)/T_w = -0.2$

$(T_w - T_0)/T_w = 0.2$

$(T_w - T_0)/T_w = 0.6$

$(T_w - T_0)/T_w = 0.75$
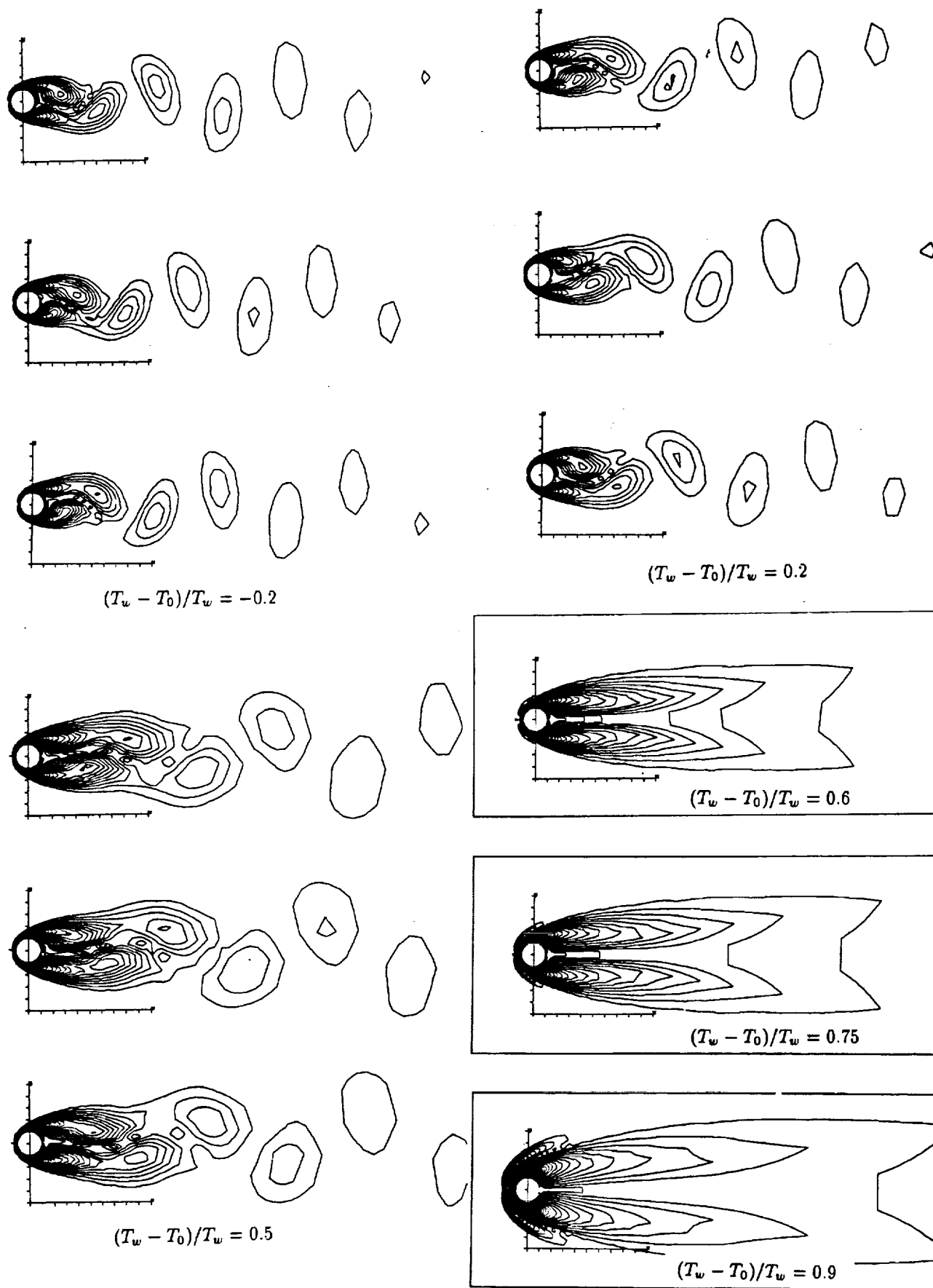
$(T_w - T_0)/T_w = 0.5$

$(T_w - T_0)/T_w = 0.9$

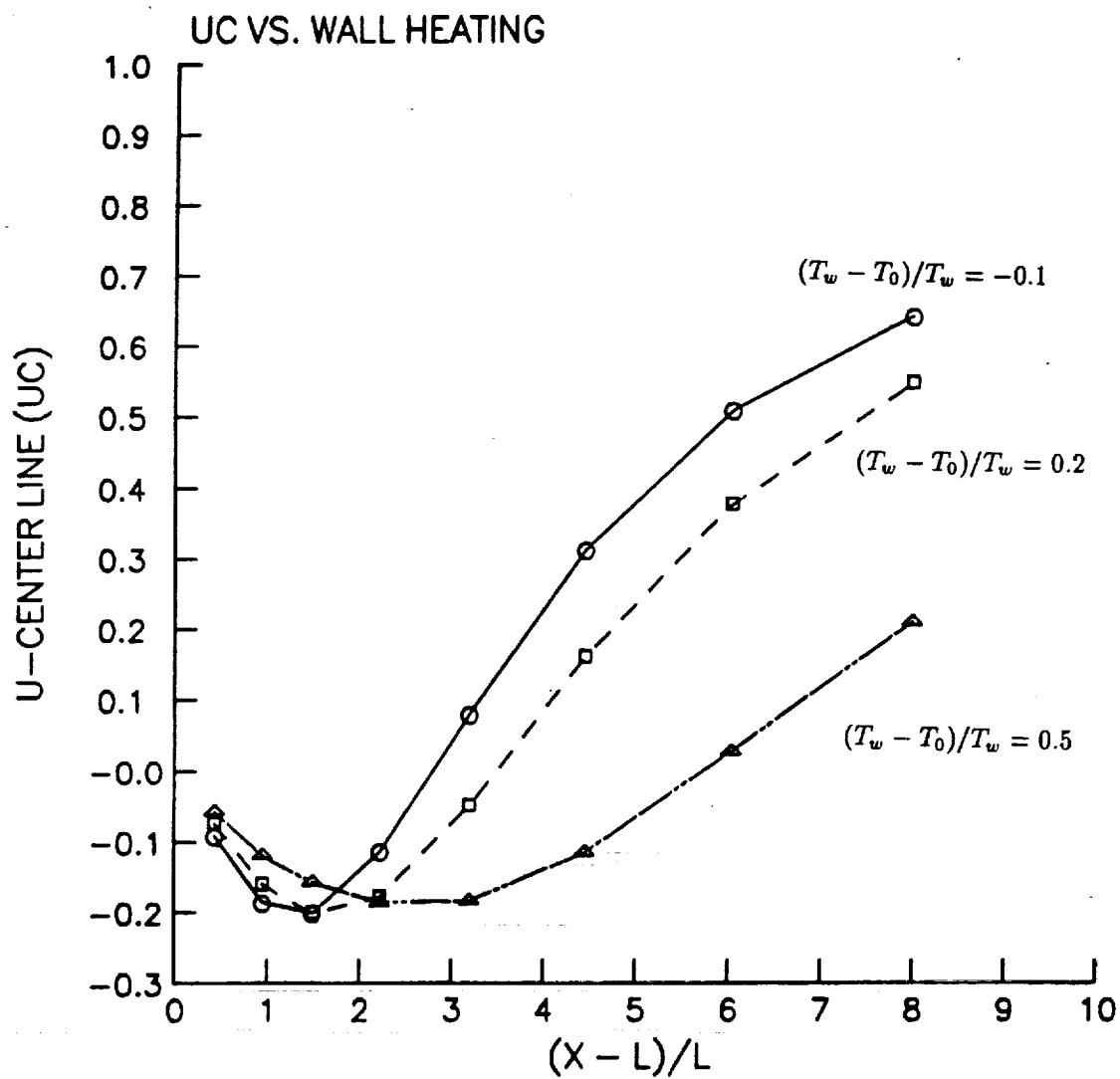Figure 18. Contours of vorticity magnitude. $Re_d$=100, $M_\infty$=0.3.

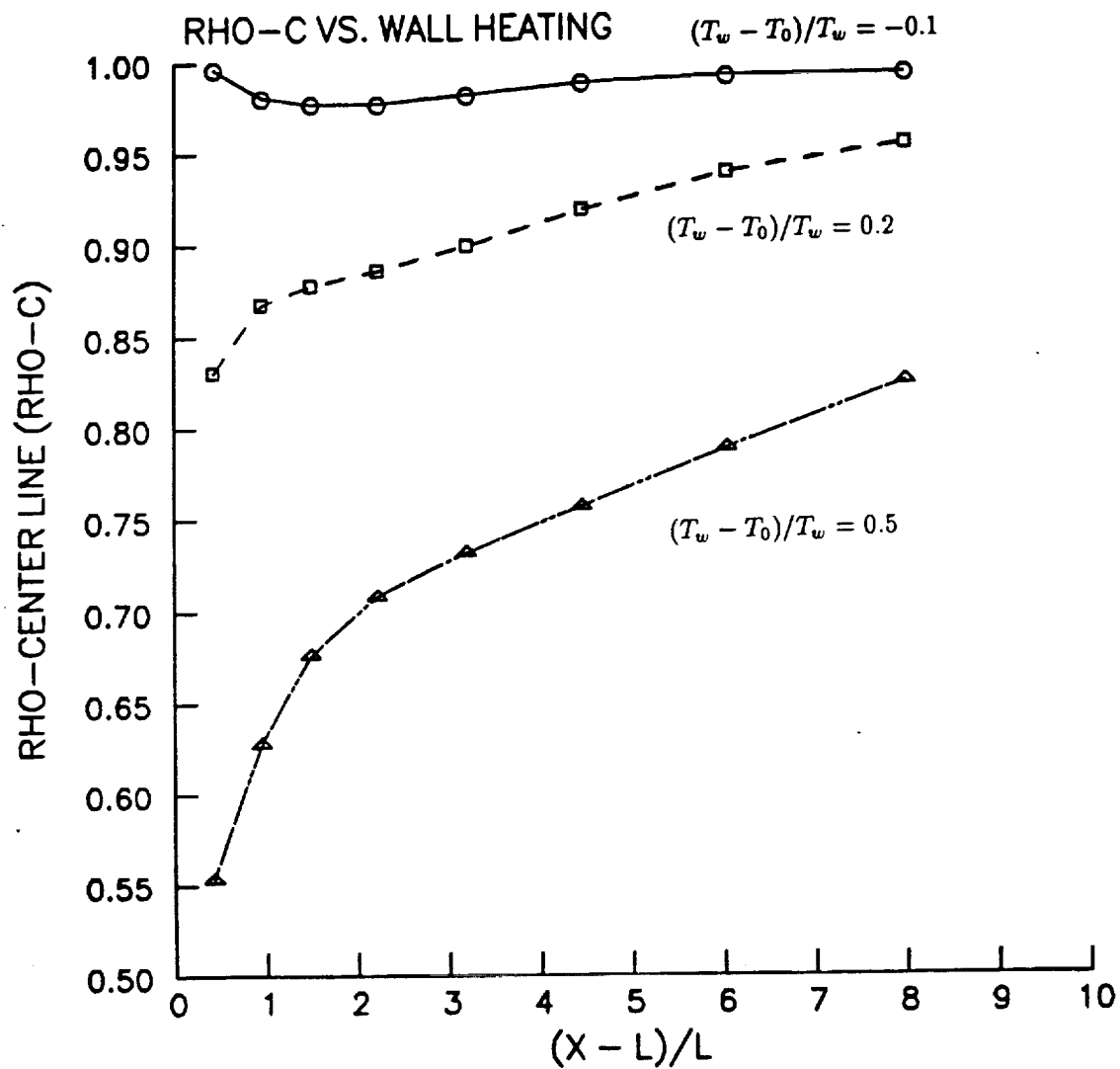Figure 19. Centerline velocities ($U_c/U_\infty$) in the wake.

Figure 20. Centerline densities ($\rho_c/\rho_\infty$) in the wake.

# REPORT DOCUMENTATION PAGE

*Form Approved*
*OMB No. 0704-0188*

| 1. AGENCY USE ONLY (Leave blank) | 2. REPORT DATE | 3. REPORT TYPE AND DATES COVERED |
|---|---|---|
| | July 1992 | Technical Memorandum |

**4. TITLE AND SUBTITLE**

Breakdown of the Karman Vortex Street Due to Forced Convection and Flow Compressibility

**5. FUNDING NUMBERS**

WU-505-62-52

**6. AUTHOR(S)**

Shu-cheng Chen

**7. PERFORMING ORGANIZATION NAME(S) AND ADDRESS(ES)**

National Aeronautics and Space Administration
Lewis Research Center
Cleveland, Ohio 44135-3191

**8. PERFORMING ORGANIZATION REPORT NUMBER**

E-7212

**9. SPONSORING/MONITORING AGENCY NAMES(S) AND ADDRESS(ES)**

National Aeronautics and Space Administration
Washington, D.C. 20546-0001

**10. SPONSORING/MONITORING AGENCY REPORT NUMBER**

NASA TM-105853

**11. SUPPLEMENTARY NOTES**

Responsible person, Shu-cheng Chen, (216) 433-8640.

**12a. DISTRIBUTION/AVAILABILITY STATEMENT**

Unclassified - Unlimited
Subject Category 34

**12b. DISTRIBUTION CODE**

**13. ABSTRACT (Maximum 200 words)**

Low speed compressible flow around a heated/cooled circular cylinder has been investigated. The phenomenon of sudden disappearing of the Karman vortex street, observed in the experiment of Noto et al., was numerically simulated and studied. It was found that breakdown of the vortex street at $Re_d = 100$ and $M_\infty = 0.3$ is primarily an effect of forced convection. The contribution of natural convection to the current event is inconsequential. The exact mechanism of this phenomenon is unknown. However, the reason for the breakdown of vortex street is believed to be due to a high temperature zone in the wake generated by high level of wall heating. This produces an effectively lower Reynolds number flow in the near wall region when a compressible gaseous media is used. Vortex shedding stops for a reason similar when flow Reynolds number is reduced globally below its minimum value. These contrast to the results of Noto et al., who argued that the buoyancy effect was the driving mechanism of the vortex breakdown. In a current study, periodic vortex sheddings were observed when the wall heating ratio was less than 0.6. In that region, the coefficient of lift decreased sharply to zero, drag increased slowly, and the Strouhal number and Nusselt number reduced monotonically with respect to the wall heating. When the heating ratio was greater than or equal to 0.6, vortex shedding stopped. And steady flows with symmetric twin trailing vortices were observed. In the region, both lift and Strouhal number remained zero, the drag increased sharply, and the Nusselt number maintained the same decreasing slope as the one obtained from the previous region. Many of these characteristics are instinctively different from the numerical results presented by Chang and Sa, who simulated the vortex breakdown phenomenon by using a mathematical model for an incompressible buoyancy dominated flow. In this paper, quantitative results such as Strouhal number, lift, drag, and Nusselt number, as well as qualitative results such as streamline, isothermal, and vorticity contours obtained at various flow conditions are presented and compared with results of Noto et al. and Chang et al.. Contrasts between the two are discussed.

**14. SUBJECT TERMS**

Vortex shedding; Vortex breakdown; Forced convection; Compressible flow

**15. NUMBER OF PAGES**

40

**16. PRICE CODE**

A03

| 17. SECURITY CLASSIFICATION OF REPORT | 18. SECURITY CLASSIFICATION OF THIS PAGE | 19. SECURITY CLASSIFICATION OF ABSTRACT | 20. LIMITATION OF ABSTRACT |
|---|---|---|---|
| Unclassified | Unclassified | Unclassified | |